

1
2
3
4
5
6
7
8
9
10
11
12
13
14
15
16
17
18
19
20
21
22
23
24
25
26
27
28
29
30

Revision 1

**Allendeite (Sc₄Zr₃O₁₂) and hexamolybdenum (Mo,Ru,Fe), two new minerals from
an ultrarefractory inclusion from the Allende meteorite**

Chi Ma*, John R. Beckett, George R. Rossman
Division of Geological and Planetary Sciences
California Institute of Technology
Pasadena, CA 91125, USA

ABSTRACT

During a nanomineralogy investigation of the Allende meteorite with analytical scanning electron microscopy, two new minerals were discovered; both occur as micro- to nano-crystals in an ultrarefractory inclusion, *ACM-1*. They are allendeite, Sc₄Zr₃O₁₂, a new Sc- and Zr-rich oxide; and hexamolybdenum, (Mo,Ru,Fe,Ir,Os), a Mo-dominant alloy. Allendeite is trigonal, $R\bar{3}$, $a = 9.396 \text{ \AA}$, $c = 8.720 \text{ \AA}$, $V = 666.7 \text{ \AA}^3$, and $Z = 3$, with a calculated density of 4.84 g/cm^3 via the previously described structure and our observed chemistry. Hexamolybdenum is hexagonal, $P6_3/mmc$, $a = 2.7506 \text{ \AA}$, $c = 4.4318 \text{ \AA}$, $V = 29.04 \text{ \AA}^3$ and $Z = 2$, with a calculated density of 11.90 g/cm^3 via the known structure and our observed chemistry. Allendeite is named after the Allende meteorite. The name hexamolybdenum refers to the symmetry (primitive hexagonal) and composition (Mo-rich). The two minerals reflect conditions during early stages of the formation of the solar system. Allendeite may have been an important ultrarefractory carrier phase linking Zr-, Sc- oxides to the more common Sc-, Zr-enriched pyroxenes in Ca-Al-rich inclusions. Hexamolybdenum is part of a continuum of high temperature alloys in meteorites supplying a link between Os- and/or Ru-rich and Fe-rich meteoritic alloys. It may be a derivative of the former and a precursor of the latter.

31 **Keywords:** allendeite, $\text{Sc}_4\text{Zr}_3\text{O}_{12}$, hexamolybdenum, new alloy, new mineral, EBSD,
32 nanomineralogy, Allende meteorite, CV3 carbonaceous chondrite.

33 -----

34 *E-mail: chi@gps.caltech.edu

35

36 INTRODUCTION

37 Processes that occurred during the first few million years of our solar system
38 are largely inferred from the study of meteorites and their constituents (e.g., Kerridge
39 and Matthews 1988; Lauretta and McSween 2006). Where the elements and/or
40 isotopes in a mineral are fractionated or one phase is stabilized over another, it is
41 often possible to constrain the nature of the environment and/or the intensity of the
42 process(es) that led to these fractionations and changes in stability. Thus, each new
43 phase adds a new voice and, with appropriate thermodynamic and/or kinetic data, it
44 may be also possible to understand some of the lyrics.

45 The Allende meteorite, which fell near Pueblito de Allende, Chihuahua,
46 Mexico on February 8, 1969, is a CV3 carbonaceous chondrite. It is the largest
47 carbonaceous chondrite ever recovered on the Earth and is often called the best-
48 studied meteorite in history. More than four decades after it fell, this meteorite
49 continues to be the source of new discoveries. For example, in the first decade after
50 its fall, Allende yielded at least seven minerals not previously observed in meteorites
51 (Fuchs 1969, 1971; Keil and Fuchs 1971; Fuchs and Blander 1977; Lovering et al.
52 1979) and, in the last several years, Allende has yielded another 18 minerals new to
53 meteorites, twelve of which are also new to science (Ma 2010, 2013a,b; Ma and
54 Rossman 2008b, 2009a,b,c; Ma and Krot 2013; Ma et al. 2009b, 2012,
55 2013a,b,c,2014; this work). Overall, Allende, one of nearly forty thousand known
56 meteorites, is the original source of nearly one in ten of the known minerals in
57 meteorites (cf., Rubin 1997). In this work, we describe two of these new minerals,
58 allendeite and hexamolybdenum, which were discovered in an Allende
59 ultrarefractory inclusion, named *ACM-1*. We describe the properties and chemistry
60 of both phases and explore their origin and evolution. Preliminary results of the
61 work reported in this study are given by Ma et al. (2009a).

62

63

MINERAL NAMES AND TYPE MATERIALS

64

65

66

67

68

69

70

71

72

73

74

75

76

77

78

79

80

81

82

83

OCCURRENCE AND ASSOCIATED MINERALS

84

85

86

87

88

89

90

91

92

The section containing the holotype allendeite specimen was prepared from a 1-cm-diameter fragment of Allende (Caltech Meteorite Collection No. Allende-12A) and deposited in the Smithsonian Institution's National Museum of Natural History under catalog number USNM 7554. The holotype hexamolybdenum specimen described in the text, a 1.2 μm crystal occurring with allendeite in USNM 7554, was the crystal most amenable to detailed characterization but the grain was lost during the attempted ion probe analysis of an adjacent grain. Additional specimens of hexamolybdenum can, however, be found in the Smithsonian Institution's National Museum of Natural History Allende section USNM 3509HC12 and in section USNM 7590 of NWA 1934, another CV3 chondrite. Some of the refractory alloy grains from acid residues of the Murchison CM2 chondrite described by Harries et al. (2012) are also hexamolybdenum.

The name allendeite refers to the host meteorite, Allende, which has proven to be a treasure trove of new minerals, as noted above, and is the target of many important studies on the origin and evolution of the solar system. The name hexamolybdenum refers to the symmetry (primitive hexagonal) and composition (Mo-rich) of this refractory alloy. The two minerals and their names have been approved by the Commission on New Minerals, Nomenclature and Classification of the International Mineralogical Association (IMA 2007-027 and IMA 2007-029).

The Allende CV3 carbonaceous chondrite fell within a strewn field near Pueblito de Allende, Chihuahua, Mexico on February 8, 1969 (Clarke et al. 1970). The minerals allendeite and hexamolybdenum were both found within one ovoid-shaped $\sim 70 \mu\text{m} \times 120 \mu\text{m}$ ultrarefractory inclusion in one polished section (USNM 7554) of this meteorite (Fig. 1). We used electron backscatter diffraction (EBSD), discussed below, to determine the orientation of crystals in the section and this shows that allendeite ($\text{Sc}_4\text{Zr}_3\text{O}_{12}$) in the upper portion of Fig. 1 (Fig. 2) forms a single $15 \times 25 \mu\text{m}$ crystal with included perovskite, Os-Ir-Mo-W alloys, and Sc-stabilized tazheranite (cubic zirconia). There are also both linked and isolated 1-5 μm irregular

93 grains, coexisting with perovskite, hexamolybdenum (Mo,Ru,Fe,Ir,Os), and other
94 Os-, Ir-, Mo-, Ru-, W-rich alloys elsewhere in the inclusion. *ACM-1* is largely altered
95 to nepheline, sodalite and an aluminous, low-Ti augite, with surviving allendeite
96 invariably in contact with perovskite. Allendeite - nepheline contacts appear sharp
97 and the allendeite does not appear to be embayed. Perovskite, where in contact with
98 alteration phases, is often rimmed by ilmenite. We also observed one grain of Mg-Al
99 spinel in contact with allendeite, hexamolybdenum, and perovskite, and rare Fe-Mg-
100 Al spinels in the altered regions of the inclusion.

101 Euhedral hexamolybdenum was initially investigated because it combined strong
102 backscattered electron intensity with clear crystal shapes that contrasted with the anhedral
103 habits of other alloy grains in the same inclusion (Fig. 3). This phase occurs as inclusions
104 in allendeite and a Zr-, Y-rich perovskite in USNM 7554. Other Os-Ir-Mo-Ru-W-bearing
105 alloys in which Mo is not the dominant element, tazheranite (Zr,Sc,Ca,Ti)O_{1.75}, and
106 spinel are observed within 2 μm (Figs. 1-3; Tables 1-2). Like hexamolybdenum, the
107 more Os-W-Ir enriched alloys in this inclusion have strong backscatter electron
108 intensities but they are invariably anhedral. In USNM 3509HC12, euhedral
109 hexamolybdenum is included in Ti-, Sc-enriched kushiroite and is associated with
110 perovskite.

111 The 1.2 μm diameter grain of hexamolybdenum in *ACM-1* consists of two
112 compositionally distinct portions. The upper, larger portion of the crystal (Fig. 3b) is a
113 Mo-dominant (hexamolybdenum) phase and the lower brighter (higher Z) part is
114 sufficiently enriched in Ru to be the mineral ruthenium. Analysis by EPMA (Table 2)
115 shows the hexamolybdenum portion of this crystal to have an empirical formula of
116 Mo_{0.56}Ru_{0.24}Fe_{0.08}Ir_{0.07}Os_{0.03}W_{0.01}Ni_{0.01} and the lower, brighter portion Ru_{0.41}Mo_{0.39}Ir_{0.10}
117 Fe_{0.05}Os_{0.03}W_{0.01}Ni_{0.01}. From EBSD analysis shows that both portions have the same
118 hexagonal structure. The apparently sharp discontinuity in composition suggests either
119 episodic growth or exsolution. The two smaller hexamolybdenum grains shown in Fig. 3
120 are too small for quantitative EPMA but SEM-EDS analysis yielded Mo_{0.44}Ir_{0.26}
121 Ru_{0.19}Fe_{0.06}W_{0.04}Os_{0.01} (larger grain) and Mo_{0.82}Ru_{0.08}Fe_{0.04}Os_{0.03}W_{0.02}Ir_{0.01} (smaller grain).
122 The larger of the two grains was confirmed to be hexamolybdenum by SEM-EDS and
123 EBSD. The simplified formula of hexamolybdenum is: (Mo, Ru, Ir, Fe, W, Os).

124

125

APPEARANCE, PHYSICAL, AND OPTICAL PROPERTIES

126

127

128

129

130

131

132

Allendeite occurs as anhedral grains, as large as $10 \times 25 \mu\text{m}$ in section. Color, streak, luster, hardness, tenacity, cleavage, fracture, density and refractive index were not determined because of the optically thick section holding the sample and the small grain size. The density, calculated from the empirical formula (Table 1) and the structure as given by Rossell (1976) is 4.84 g/cm^3 . Allendeite is not cathodoluminescent under the electron beam of a scanning electron microscope and we observed no crystal forms or twinning.

133

134

135

136

137

138

139

Hexamolybdenum occurs in *ACM-I* as euhedral, metallic grains, $0.2 - 1.2 \mu\text{m}$ in diameter (Figs. 1, 3). Color, streak, luster, hardness, tenacity, cleavage, fracture, and density could not be determined because of the small grain size. The calculated density is 11.90 g/cm^3 via the structure of Anderson and Hume-Rothery (1960) and our observed chemistry (Table 2). Hexamolybdenum is not cathodoluminescent under the electron beam of an SEM.

140

CHEMICAL COMPOSITION

141

142

143

144

145

146

147

148

149

150

151

152

153

Backscatter electron (BSE) images were obtained with a ZEISS 1550VP field emission SEM and a JEOL 8200 electron microprobe using solid-state BSE detectors. Quantitative elemental microanalyses of allendeite, hexamolybdenum, and associated grains were conducted with the JEOL 8200 electron microprobe operated in a focused beam mode at 15 kV and 10 nA for allendeite and 5 nA for hexamolybdenum. Standards for the analysis of allendeite and associated oxides and silicates were zircon ($ZrL\alpha$), $ScPO_4$ ($ScK\alpha$), YPO_4 ($YL\alpha$), Hf metal ($HfL\alpha$), anorthite ($CaK\alpha$, $AlK\alpha$, $SiK\alpha$), albite ($NaK\alpha$), microcline ($KK\alpha$), fayalite ($FeK\alpha$), forsterite ($MgK\alpha$), TiO_2 ($TiK\alpha$), V_2O_5 ($VK\alpha$), Cr_2O_3 ($CrK\alpha$) and sodalite ($ClK\alpha$). Standards for the analysis of hexamolybdenum were the pure metals Mo ($K\alpha$), Fe ($K\alpha$), W ($L\alpha$), Ru ($L\alpha$), Os ($L\alpha$), Ir ($L\alpha$), Ni ($K\alpha$), Pt ($L\alpha$), and Re ($L\alpha$). Quantitative elemental microanalyses were processed with the CITZAF correction procedure (Armstrong 1995) and analytical results are given in Tables 1-2. An Oxford INCA X-ray energy dispersive spectrometer (EDS) on the ZEISS SEM was also

154 used for elemental analysis. These data were processed using the XPP correction
155 procedure of Pouchou and Pichoir (1991).

156 The average of eight electron probe microanalyses (EPMA) of allendeite crystals
157 (Table 1) leads to an empirical formula referenced to twelve oxygens of
158 $(\text{Sc}_{3.01}\text{Ti}^{4+}_{0.44}\text{Ca}_{0.31}\text{Al}_{0.09}\text{Fe}^{2+}_{0.07}\text{Y}_{0.04}\text{V}^{3+}_{0.03})_{\Sigma 3.99}(\text{Zr}_{2.95}\text{Hf}_{0.04})_{\Sigma 2.99}\text{O}_{12}$. No other elements
159 with atomic number greater than 4 were detected by WDS scans. Given the close
160 adherence to an $\text{X}_4\text{Z}_3\text{O}_{12}$ stoichiometry and the fact that the number of cations of Ti
161 (0.44) in the formula unit is approximately equal to $\text{Ca}^{2+} + \text{Fe}^{2+}$ (0.40), Ti is dominantly
162 tetravalent, although we can't exclude the presence of minor amounts of trivalent Ti
163 (<~15% of the total). Assuming that Ti is quadrivalent, allendeite in ACM-1 can be
164 treated, to first order, as a solid solution $\text{Sc}_4\text{Zr}_3\text{O}_{12} - (\text{X}^{2+}\text{Ti}^{4+})_2\text{Zr}_3\text{O}_{12} - \text{Z}^{3+}_4\text{Zr}_3\text{O}_{12}$,
165 where X refers to divalent cations, Z refers to all trivalent cations other than Sc, and Hf is
166 ignored for simplicity. The $\text{Sc}_4\text{Zr}_3\text{O}_{12}$ component comprises ~85 mole % of allendeite in
167 *ACM-1*.

168 Figure 4 shows the compositions of allendeite and other Sc-, Zr-enriched phases
169 from carbonaceous chondrites. Allendeite is Sc-enriched relative to tazheranite in *ACM-*
170 *I* and other zirconias reported in the literature, with the exception of one described by
171 Weber and Bischoff (1994) from a perovskite-rich, grossite-bearing inclusion in the CH
172 chondrite Acfer 182. Based on the close compositional similarity to allendeite, this phase
173 is probably allendeite and not an unusually Sc-rich tazheranite. Panguite and kangite are
174 more titaniferous than allendeite and considerably poorer in Sc and Zr.

175 Compositions of allendeite, hexamolybdenum and associated phases in *ACM-I*
176 are given in Tables 1-2. The oxides are highly enriched in Sc. Tazheranite (15 wt %
177 Sc_2O_3) is Sc-rich relative to the meteoritic zirconias reported by other workers [Noonan
178 et al. 1977; Lovering et al. 1979; Hinton et al. 1988; based on composition, we interpret
179 the Sc-, Zr-rich oxide from inclusion 418/P in Acfer 182 described by Weber and
180 Bischoff (1994) as allendeite (i.e., not as tazheranite)]. The included perovskite in *ACM-I*
181 $[(\text{Ca}_{0.89}\text{Y}_{0.08}\text{Sc}_{0.04})_{1.01}(\text{Ti}_{0.88}\text{Zr}_{0.06}\text{Al}_{0.05}\text{Fe}_{0.01})_{1.00}\text{O}_3; 2.5 \text{ wt } \% \text{Sc}_2\text{O}_3]$ has much less Sc
182 than the tazheranite but it is more Sc-rich than any previous perovskite composition
183 reported in the literature [none to our knowledge exceeding the 1.75 wt % Sc_2O_3 for a
184 perovskite from inclusion 418/P, which also contains Sc-rich oxides (Weber and Bischoff

185 1994)]. Compositions of the Os-Ir-Mo-W alloy grains indicated by arrows in Fig. 2 are,
186 via SEM-EDS: ($\text{Os}_{0.65}\text{Ir}_{0.14}\text{W}_{0.13}\text{Mo}_{0.05}\text{Fe}_{0.02}\text{Ru}_{0.01}$), ($\text{Os}_{0.51}\text{Ir}_{0.25}\text{W}_{0.13}\text{Mo}_{0.07}\text{Fe}_{0.02}\text{Ru}_{0.02}$),
187 and ($\text{Ir}_{0.37}\text{Os}_{0.35}\text{W}_{0.12}\text{Mo}_{0.12}\text{Fe}_{0.02}\text{Ru}_{0.02}$). The first two grains are osmiums assuming the
188 structure, which was not checked, is $P6_3/mmc$, as is observed for all other osmium-rich
189 alloys in this and other refractory inclusions in carbonaceous chondrites (Harries et al.
190 2012; this study). The third grain is sufficiently Ir-enriched to be an iridium, if it is cubic,
191 or, despite the very low Ru content, a rutheniridosmine if it is hexagonal. The osmiums
192 in *ACM-I* are the most Os- and W-rich meteoritic alloys that we are aware of, aside from
193 grains in a lakargiite (CaZrO_3)-bearing inclusion from Acfer 094 (Ma 2011). Alteration
194 phases include sodalite and nepheline. Perovskite in direct contact with alteration phases
195 frequently has thin ($< 1 \mu\text{m}$) rims of ilmenite, which is common on Allende perovskites
196 exposed to alteration products (e.g., Keller and Buseck 1989). The inclusion is partially
197 rimmed by a Al-rich, low-Ti augite.

198

199

CRYSTALLOGRAPHY

200 Single-crystal electron backscatter diffraction (EBSD) analyses at a sub-
201 micrometer scale were performed using an HKL EBSD system on the ZEISS 1550VP
202 scanning electron microscope operated at 20 kV and 4 nA in a focused beam with a 70°
203 tilted stage in variable pressure mode (20 Pa). The EBSD system was calibrated using a
204 single-crystal silicon standard. The structure was determined and cell constants were
205 obtained by matching the experimental EBSD pattern with known structures of synthetic
206 phases. The HKL software automatically suggests indexing solutions ranked by the
207 lowest 'mean angular deviation' (MAD) with MAD numbers below 1 considered
208 desirable for accurate solutions. We used the highest ranked solutions (lowest MAD) for
209 establishing structural matches and obtained MAD numbers of 0.1 - 0.3 for allendeite,
210 and 0.3 - 0.4 for hexamolybdenum.

211

Allendeite

212 Under most conditions, EBSD can't be used to determine accurate cell parameters
213 but matches against known structures can be tested very accurately. Electron backscatter
214 diffraction (EBSD) patterns of allendeite determined in the SEM were matched against
215

216 all of the known structures of synthetic $\text{Sc}_4\text{Zr}_3\text{O}_{12}$ (Thornber et al. 1968; Rossell 1976;
217 Red'ko and Lopato 1991) and the structure of perovskite (Pawar 1967). The EBSD
218 pattern (Fig. 5) was an excellent match to the computed EBSD pattern and cell
219 parameters of synthetic $\text{Sc}_4\text{Zr}_3\text{O}_{12}$ (ICSD collection code 009615, PDF 71-1022) from
220 Rossell (1976), with the MAD numbers as low as 0.12. Alternative structures had much
221 higher MAD values (>0.6). Allendeite is trigonal with space group: $R\bar{3}$, $a = b = 9.363 \text{ \AA}$,
222 $c = 8.720 \text{ \AA}$, $V = 666.7 \text{ \AA}^3$, and $Z = 3$. Note that errors on the cell parameters are not
223 stated because they are taken directly from the data of the matching $\text{Sc}_4\text{Zr}_3\text{O}_{12}$ phase in
224 Rossell (1976). Allendeite has a fluorite-related superstructure. Zirconium and Sc are
225 both seven-coordinated to oxygen, on average, and randomly distributed over two sets of
226 general sites. The calculated density is 4.84 g/cm^3 using the observed chemistry (Table
227 1) and the cell parameters of Rossell (1976). X-ray powder-diffraction data (in Å for
228 $\text{CuK}\alpha_1$) taken from PDF 71-1022 show that the strongest calculated lines are [d in Å ,
229 intensity in % relative to that of $(12\bar{1})$, (hkl)]: [2.900 (100) ($12\bar{1}$)], [1.776 (32) (140)],
230 [1.779 (27) ($12\bar{4}$)], [1.515 (19) (143)], [2.513 (18) ($21\bar{2}$)], [4.698 (5) (110)], [1.450 (4)
231 ($21\bar{2}$)], and [1.152 (4) (701)].

232

233 **Hexamolybdenum**

234 The hexamolybdenum crystals were too small for conventional single-crystal
235 XRD study but it was possible to study them using EBSD. The EBSD patterns can be
236 indexed in terms of the $P6_3/mmc$ structure exhibited by Ru (Urashima et al. 1974) and
237 some intermediate Ru-Mo alloys (Anderson and Hume-Rothery 1960; Kraus and Nolze
238 1996; Park et al. 2000) but not in terms of the cubic $Im\bar{3}m$ structure assumed by Mo
239 (Kleykamp 1988) or tetragonal $P4_2/mnm$ Mo-Ru structures (Raub 1954; Anderson and
240 Hume-Rothery 1960; Park et al. 2000). The best fit was achieved using cell parameters of
241 synthetic $\text{Mo}_{55}\text{Ru}_{45}$ (e.g., Anderson and Hume-Rothery 1960) (Fig. 6), with mean angular
242 deviations as low as 0.27. Hexamolybdenum is hexagonal with space group $P6_3/mmc$, $a =$
243 2.7506 \AA , $c = 4.4318 \text{ \AA}$, $V = 29.04 \text{ \AA}^3$ and $Z = 2$. It has the same crystal structure as the
244 minerals garutiite (Ni,Fe,Ir), hexaferrum (Fe,Os,Ru,Ir), ruthenium (Ru,Ir,Os),
245 rutheniridosmine (Ir,Os,Ru), and osmium (Os,Ir). The X-ray powder-diffraction data (in

246 Å for $\text{CuK}\alpha_1$) calculated with the empirical formula using the program Powder Cell
247 version 2.4 (e.g., Kraus and Nolze 1996), reveals that the strongest calculated lines are [d
248 in Å, intensity in % relative to that of (101), (hkl)]: [2.098, (100), (101)], [2.216, (26),
249 (002)], [2.382, (24), (100)], [1.169, (20), (112)], [1.255, (18), (103)], [1.375, (17), (110)],
250 [1.622, (15), (102)], and [1.150 (14) (201)].

251 In addition to the grains in *ACM-1* described above, we also observed one 650 nm
252 inclusion of hexamolybdenum in perovskite from a fine-grained inclusion in Allende
253 section USNM 3509HC12 (Fig. 7). This crystal has a composition of
254 $(\text{Mo}_{0.258}\text{Fe}_{0.255}\text{Ru}_{0.231}\text{Os}_{0.109}\text{Ir}_{0.094}\text{Ni}_{0.027}\text{W}_{0.020}\text{Re}_{0.006})$, as shown in Table 2, and an EBSD
255 pattern that can only be indexed with the $P6_3/mmc$ structure. Compositions of the
256 associated phases, perovskite and pyroxene are given in Table 1. Euhedral
257 hexamolybdenum crystals were also identified as inclusions in krotite and grossite in
258 *Cracked Egg*, a CAI from the NWA 1934 CV3 chondrite [USNM section 7590; see Fig.
259 3 in Ma et al. (2011)].

260 Molybdenum-rich alloys have been observed previously by El Goresy et al.
261 (1978) and, more recently, by Berg et al. (2010) and Harries et al. (2012), the latter
262 showing that a compositionally wide spectrum of refractory alloys from Murchison have
263 a $P6_3/mmc$ structure. This is a key characteristic for these minerals. The mineral name
264 for a particular refractory alloy grain in a carbonaceous chondrite then devolves to a
265 name associated with the element present in the highest concentration, even if it
266 constitutes less than 50% of the atoms present. Table 3 shows the current nomenclature
267 for $P6_3/mmc$ alloy minerals. All, except for the Ni-dominant alloy garutiite and Ir-
268 dominant rutheniridosmine, have been reported in meteorites.

269 Hexamolybdenum has a $P6_3/mmc$ structure that is likely stabilized over the cubic
270 structure of elemental Mo (Kleykamp 1988) by the high concentrations of “contaminant”
271 elements. It is possible that cubic Mo-dominant alloys exist in nature. For example,
272 Bogatikov et al. (2001, 2002) described two irregular micrograins of “native
273 molybdenum” in lunar regolith samples but the structure was not determined and the
274 compositions could only be characterized as pure Mo based on SEM analyses highly
275 contaminated by host phases.

276

277

RAMAN SPECTROSCOPY

278

279

280

281

282

283

284

285

286

287

288

289

290

291

292

293

294

295

296

297

298

299

ORIGIN AND SIGNIFICANCE

300

301

302

303

304

305

306

Raman spectroscopic microanalysis was carried out using a 514.5 nm laser in a Renishaw M1000 micro-Raman spectrometer system on domains of the sample in the polished section previously identified as allendeite crystals through SEM imaging and EBSD analyses. Methods are described in Ma and Rossman (2008a, 2009a).

Approximately 5 mW of 514.5 nm laser illumination (at the sample) focused with a 100× objective lens provided satisfactory spectra. The spot size was about 2 μm (i.e., roughly the size of the largest inclusion free portions of crystals). Peak positions were calibrated against a silicon standard. A dual-wedge polarization scrambler was used in the laser beam for all spectra to reduce the effects of polarization.

The Raman spectra of allendeite and the synthetic Sc₄Zr₃O₁₂ of Michel et al. (1976) in Figure 8 both show bands in the 700-200 cm⁻¹ region but the similarity is not strong. Furthermore, the allendeite spectrum shows strong bands in the 1100-900 cm⁻¹ region that are absent in Sc₄Zr₃O₁₂. Bands in mineral spectra in this region can reflect laser-induced luminescence of rare-earth elements, a problem encountered with other meteoritic Sc- and Y-enriched phases (e.g. Ma et al. 2013c). We did not detect rare earth elements via EPMA but laser-induced luminescence can be generated by concentration of the rare earths that are far below the electron microprobe detection limits (Gaft et al. 2005). We conclude that many, and possibly most, of the features of the Raman spectrum of allendeite are caused by rare-earth luminescence rather than arising from intrinsic features of the mineral, itself.

A number of minerals with high scandium contents have been found in meteorites including davisite, panguite, kangite, tazheranite, thortveitite, and allendeite. Allendeite is the most Sc-rich of these phases (32.4 wt. % Sc₂O₃) and only pretulite, ScPO₄, a terrestrial phosphate with 49.3 wt. % Sc₂O₃, has a substantially more Sc.

Hexamolybdenum is part of a continuum of meteoritic refractory alloys with the P6₃/mmc structure that is summarized in Table 3. The mineral names are more obviously descriptive than genetic but there is value in the nomenclature because the names reflect

307 differences in chemistry that connect to the history of the mineral and, therefore, to the
308 history of the host inclusion. In this section, we consider the origin and evolution of
309 *ACM-I* through its constituent phases, particularly of allendeite and hexamolybdenum.

310 An initial clue to the formation of *ACM-I* lies in the compositions of the
311 constituent phases and the bulk composition of the inclusion. From Fig. 1, the inclusion
312 is heavily altered to a mixture of nepheline, sodalite, and augite. Perovskite appears to
313 have survived the alteration event intact, except for some thin ilmenite rims where grains
314 are in contact with alteration phases but allendeite is apparently destroyed as it is
315 observed only where partially protected by perovskite. It is possible that other pre-
316 alteration phases comprised the bulk of what is now alteration products but we see no
317 traces of them, whereas residual allendeite is common within the altered region
318 interstitial to perovskite.

319 To construct a mode for the precursor inclusion prior to alteration, we begin with
320 perovskite because it is the primary phase least affected by the alteration process.
321 Ignoring possible increases in the volume of the inclusion due to alteration, a point count
322 from Fig. 1 yields 24 volume % perovskite. Tazheranite is observed only in the large
323 allendeite grain shown in Fig. 1. If this is representative of the inclusion as a whole, prior
324 to alteration, then there was ~ 2 volume % tazheranite. Refractory alloy grains can
325 survive the Allende alteration process(es), although compositions are affected (Paque et
326 al. 2008). However, we observed refractory alloys only as inclusions in allendeite or
327 perovskite (i.e., not in the altered regions). We assume that this reflects plucking during
328 section preparation and use the same approach for platinum group element (PGE)
329 enriched alloys that we did for tazheranite, yielding ~1% by volume for the inclusion. If
330 the balance of the inclusion was originally allendeite, then the pre-alteration mode of
331 *ACM-I* was 73% allendeite, 24% perovskite, 2% tazheranite and 1% alloy (i.e.,
332 neglecting the trace spinel). Given average compositions for the phases in *ACM-I*
333 (Tables 1-2) and the densities for allendeite and hexamolybdenum (this study), perovskite
334 (Robie et al. 1979), and tazheranite (Konev et al. 1969; see summary in English in
335 Fleischer 1970), bulk enrichments relative to CI chondrites are 0.5 (Al with spinel
336 neglected), 7 (Ca), 7,000 (Y), 30,000 (Sc), 80,000 (Hf), and 90,000 (Zr) for the refractory
337 lithophile elements and 9,000 – 19,000 for Mo, W, Ir, and Os. For individual Mo-Os-W

338 grains, enrichments relative to CI abundances reach 10^5 . Although we have not explored
339 REE abundances in the primary minerals, it seems fair to say that *ACM-I* is an
340 ultrarefractory inclusion.

341

342 **Allendeite and Tazheranite**

343 It has long been known that Zr-oxides are extremely refractory in nebular
344 environments as ZrO_2 is the highest temperature oxide to appear in condensation
345 calculations for a cooling gas of solar composition (Grossman 1973; Lodders 2003).
346 Condensation calculations imply that Sc, although quite refractory, is volatile relative to
347 ZrO_2 (Grossman 1973; Kornacki and Fegley 1986; Lodders 2003) with Grossman (1973)
348 calculating the initial condensation of Sc_2O_3 , which is not observed in meteorites,
349 Kornacki and Fegley (1986) assuming that Sc condensed in an ideal molecular solution
350 of Sc_2O_3 in $CaTiO_3$ perovskite (meteoritic perovskites can have wt % level concentrations
351 of Sc_2O_3 ; e.g., Table 1) and Lodders (2003) assigning Sc to hibonite, which condenses at
352 higher temperatures than perovskite. The highly refractory ZrO_2 has a higher
353 condensation temperature than other refractory oxides and undoubtedly accommodates
354 some Sc but the CI ratio for Sc_2O_3/ZrO_2 is 3.4 by weight, so that, even if condensate
355 tazheranites were all as Sc-rich as the zirconia in *ACM-I* (Table 1), which is unusually
356 scandian, only a small fraction of the Sc in a cooling gas of solar composition could be
357 accounted for through solid solution in zirconia. A similar consideration holds for
358 allendeite ($Sc_2O_3/ZrO_2 \sim 0.6$).

359 There are a variety of rare Sc-enriched phases in carbonaceous chondrites but
360 most Sc is probably sequestered as a minor to trace element in more common phases.
361 For example, meteoritic hibonites have variable but small concentrations of Sc [18-1316
362 ppm by weight with an average of 277 ppm for data of Hinton et al. (1988), Ireland et al.
363 (1988, 1991), Sahijpal et al. 2003, and Simon et al. 2002) but these are in the general
364 range needed to account for a solar Sc/Al ratio (~ 600 ppm Sc). It is likely that hibonite is
365 a significant sink for Sc in nebular settings. Scandium-, Zr-enriched pyroxenes including
366 davisite are not considered in condensation calculations because the thermodynamic
367 properties have not been studied. Also, it is worth noting that, although some Sc-, Zr-
368 enriched oxides may have originated as condensates, crystallization needs to be

369 considered for those occurring in igneous types A and B CAIs (Simon et al. 1991; El
370 Goresy et al. 2002)

371 Tazheranite can potentially be used as a sensitive indicator of environment
372 through vapor – solid reactions of the type $2\text{ScO}_{(g)} + \frac{1}{2}\text{O}_{2(g)} = \text{Sc}_2\text{O}_{3(\text{Taz})}$, where “Taz”
373 refers to tazheranite and “g” to the vapor phase, and solid – solid reactions such as
374 $\text{CaO}_{(\text{Taz})} + \text{TiO}_{2(\text{Taz})} = \text{CaTiO}_{3(\text{Pv})}$, where Pv refers to perovskite. Realizing this potential
375 is difficult because meteoritic tazheranites are compositionally complex (e.g., Table 1).
376 Even neglecting Fe as a possible alteration component, there are wt % level
377 concentrations of Ca, Zr, Hf, Y, and Ti, the latter possibly multivalent. Thus, tazheranite
378 is attractive in providing multiple statements of equilibrium relevant to environments for
379 which we have very little information but it is difficult to quantify these statements
380 because the underlying thermodynamic properties are not sufficiently well constrained.

381 Even for binary Sc-Zr oxides, there are few data constraining the thermodynamic
382 properties. Jacobson et al. (2001) assessed the system $\text{ScO}_{1.5}\text{-ZrO}_2$ based mostly on the
383 phase diagram and analogies with the much better constrained system $\text{YO}_{1.5}\text{-ZrO}_2$. They
384 treated allendeite as a line compound (i.e., composition fixed as $\text{Sc}_4\text{Zr}_3\text{O}_{12}$) and modeled
385 cubic zirconia as a binary solid solution using a Redlich-Kister formalism. The resulting
386 model yields strongly positive deviations from ideality for Sc in cubic zirconia, in
387 contrast to the strong negative deviations obtained by Belov et al. (1987), and shows only
388 fair agreement with the experimentally determined phase equilibria. For the observed
389 composition of tazheranite from *ACM-1* to be consistent with equilibration with host
390 allendeite, large differences in thermodynamic properties relative to those inferred from
391 the model of Jacobson et al. (2001) would seem to be required. For example, the model
392 of Jacobson et al. (2001) could be correct for $\text{ScO}_{1.5}\text{-ZrO}_2$ but the solution of Ti leads to
393 sharply negative deviations from ideality of the $\text{Sc}_4\text{Zr}_3\text{O}_{12}$ component in allendeite
394 (activity coefficients of $\sim 1/3$ or less would be needed). Alternatively, activity
395 coefficients of $\text{ScO}_{1.5}$ in tazheranite could be even higher, by 50% or more, than those
396 predicted by Jacobson et al.’s model or the free energy of formation of $\text{Sc}_4\text{Zr}_3\text{O}_{12}$ could
397 substantially more negative than predicted by Jacobson et al. (by 16–21kJ/mole for
398 temperatures in the range of 800-1500°C, if cubic zirconia terms were retained). Since
399 the thermodynamic assessment of Jacobson et al. simultaneously fits the thermodynamic

400 properties of all phases in the system, we cannot arbitrarily accept the model parameters
401 for one phase without accepting them for all. We have, therefore, not calculated the
402 stability of $\text{Sc}_4\text{Zr}_3\text{O}_{12}$ allendeite in nebular settings based on the thermodynamic
403 assessment of Jacobson et al. (2001). Additional constraints on the thermodynamic
404 properties of allendeite and Sc-bearing cubic zirconia are needed.

405 Allendeite is quite rare in carbonaceous chondrites as our continued surveys of
406 Sc- and Zr-enriched phases in Allende and other carbonaceous chondrites have yet to
407 yield another example; the literature contains only one occurrence, described by Weber
408 and Bischoff (1994), that we infer to be allendeite based on the composition. Davisite is,
409 by far, the most common Sc-enriched phase in carbonaceous chondrites. This suggests
410 that allendeite is either the product of a very rare environment or it forms frequently but
411 is readily destroyed through gas-phase reactions. Davisite is a possible endproduct of
412 allendeite alteration and, indeed, of the high temperature nebular alteration of any Sc-rich
413 oxide but appealing to this phase would require an additional sink for Zr as molar Sc~Zr
414 in allendeite but $\text{Sc} \gg \text{Zr}$ in davisite. Certainly, based on *ACM-I*, allendeite is unstable
415 during the alkali-iron metasomatism that altered *ACM-I* and other refractory inclusions in
416 Allende such that there was a net loss of Sc and Zr to the inclusion as there are no Sc-rich
417 phases within or around altered portions of *ACM-I*.

418 In addition to vapor – solid reactions, allendeite may also be destroyed through
419 dissolution into silicate melts. Based on the phase diagram for $\text{Sc}_2\text{O}_3\text{-ZrO}_2$, end-member
420 $\text{Sc}_4\text{Zr}_3\text{O}_{12}$ allendeite is extremely refractory. It is stable to $\sim 2100^\circ\text{C}$, where it breaks
421 down to form a Sc-rich cubic zirconia of the same composition (Jacobson et al. 2001).
422 Although the upper thermal stability limit for Ti-rich allendeites may be lower than for
423 $\text{Sc}_4\text{Zr}_3\text{O}_{12}$, it seems likely that meteoritic allendeite is thermally stable at peak
424 temperatures for CAI melting ($\sim 1400\text{-}1500^\circ\text{C}$; Stolper and Paque 1986; Richter et al.
425 2006). If so, the phase would dissolve into the melt, whether congruently (dissolving
426 allendeite-melt interface) or incongruently (intermediate phase(s) produced between
427 allendeite and melt) being indeterminate at present. Allendeite would not simply melt
428 with diffusive homogenization between CAI host melt and an allendeite composition
429 liquid.

430 If originally present in the precursor phase assemblage of an igneous CAI,
431 allendeite likely dissolves during melting, with the Sc, so released being mostly
432 incorporated into later-crystallizing pyroxene. The relatively common Zr-, Sc-enriched
433 pyroxenes in type A CAIs and in the mantles of type B1s (Simon et al. 1991; El Goresy
434 et al. 2002) could reflect a precursor Zr-Sc oxide that dissolved into the melt with some
435 of the Zr and Sc being subsequently incorporated into crystallizing pyroxene. If so, the
436 $\text{Sc}_2\text{O}_3/\text{ZrO}_2$ ratio of such a pyroxene would depend on (1) $\text{Sc}_2\text{O}_3/\text{ZrO}_2$ in the dissolving
437 phase assemblage (~ 0.6 by weight if only allendeite; lower if perovskite or tazheranite
438 are significant contributors and higher if kangite or panguite are present); (2) how much
439 diffusion occurred in the liquid prior to crystallization of the pyroxene (Sc^{3+} likely
440 diffuses more quickly than Zr^{4+} , so increased dissolution time favors lower Sc/Zr in
441 phases crystallizing in the immediate vicinity of the original Sc-, Zr-enriched phase
442 assemblage); and (3) the ratio of the pyroxene/liquid partition coefficients for Sc and Zr.
443 Taking the effective pyroxene-liquid partition coefficients for Zr (1.1) and Sc (2.8)
444 derived by Simon et al. (1991) for core pyroxenes in type B1 inclusions as approximately
445 correct for Sc-, Zr-rich clinopyroxenes in the mantle, leads to $\text{Sc}_2\text{O}_3/\text{ZrO}_2$ in initially
446 crystallizing clinopyroxene derived from dissolved allendeite of ~ 1.3 if no significant
447 diffusion of Sc relative to Zr occurred in the liquid, in reasonable agreement with
448 observed $\text{Sc}_2\text{O}_3/\text{ZrO}_2$ values (0.8-4.7; average 2.1) in pyroxenes associated with Zr-, Sc-
449 rich perovskite in compact type A inclusions (Simon et al. 1999; El Goresy et al. 2002).
450 Since allendeite has a low $\text{Y}_2\text{O}_3/\text{Sc}_2\text{O}_3$ (0.02), we would also expect low $\text{Y}_2\text{O}_3/\text{Sc}_2\text{O}_3$ in
451 the crystallizing pyroxene, also as observed (0.003 – 0.013 for data of El Goresy et al.
452 2002). Thus, allendeite is a plausible candidate for being part of a precursor phase
453 assemblage whose destruction led to the crystallization of Sc-enriched pyroxenes in
454 compact type A inclusions and in the mantles of type B1s.

455

456 **Hexamolybdenum**

457 A wide variety of refractory metal alloys are observed in Fremdlinge or opaque
458 assemblages of CAIs (El Goresy et al. 1978; Blum et al. 1989) but these probably formed
459 through oxidation/sulfidation at low temperatures of Fe-Ni-rich alloys, possibly leading
460 to exsolution of the observed refractory alloys (Blum et al. 1989). Isolated refractory

461 metal nuggets such as those in *ACM-I* are not the exsolution features of these ferrous
462 alloys. Concentrations of Fe, Ni, and the more volatile of the refractory siderophiles, Pt,
463 Rh, and V in hexamolybdenum and other alloys shown in Figs. 1-3 and 7 are quite low
464 (Table 2), as are the host phases. These alloys may be relatively pristine examples of
465 early high temperature condensates or extreme volatilization residues. The
466 euhedral/subhedral habits of hexamolybdenum in *ACM-I* and anhedral habits of those
467 alloys most enriched in Os-Ir-W may reflect a thermal event that attacked the existing
468 alloy grains prior to the condensation of most Mo and Ru (i.e., before the formation of
469 hexamolybdenum).

470 If volatility is the principal driving force behind the composition of a meteoritic
471 refractory alloys, as suggested by Berg et al. (2009) and Harries et al. (2012), among
472 many others, then the natural composition variables are (Os+W+Re), (Ir), (Mo+Ru), and
473 (Pt+Rh) because these clusters of elements form a series in order of increasing volatility
474 based on their condensation behavior (Campbell et al. 2001). In Fig. 9a, elements of
475 intermediate volatility, Ir, Ru, and Mo, are merged and alloy compositions from this
476 study and the literature are plotted in terms of the ternary (Os+W+Re) - (Ir+Mo+Ru) -
477 (Pt+Rh). Alloys from *ACM-I* are restricted to one join because they are very low in Pt
478 and Rh, implying that they are relatively refractory alloys. We expand this join in Fig.
479 9b, where Ir and Ru+Mo, the elements of intermediate volatility, have been separated
480 while still combining the most refractory metals, Os + W + Re. To zeroth order, the data
481 can be described in terms of two lines; one extending from the Os+W+Re (i.e., most
482 highly refractory) vertex towards a second line defined by alloys with chondritic
483 Ir/(Os+W+Re) ratios. From a condensation perspective, such alloys would have Ir, Os,
484 W, and Re fully condensed so that the solution of additional elements leads to the dilution
485 of more refractory elements but not to a change in their ratios). Many alloy compositions
486 are depleted in Ir in this projection and this may reflect subtleties in the thermochemistry,
487 the loss of an iridium-enriched phase in some environments, or, perhaps, systematic
488 analytical errors. Data from this study encompass a broad range of these most refractory
489 compositions (only the alloys analyzed by Ma (2011) appear to have accessed a more
490 refractory set of compositions).

491 Although the overall trends shown in Fig. 9 are consistent with the conclusions of
492 Berg et al. (2009) and Harries et al. (2012) that the alloys represent condensates, there are
493 complications inherent in the data that hint at complexities in process. For example, Fig.
494 10 shows molar Ru/Mo as a function of % Ru + Mo relative to all highly refractory
495 siderophiles, defined for present purposes as Ru+Mo+Ir+Os+W+Re. Most of the data lie
496 near a line extending from low concentrations of Ru + Mo (more refractory), with low
497 Ru/Mo, to higher concentrations of Ru + Mo (less refractory), with Ru/Mo roughly equal
498 to the CI chondrite ratio. There are, however, six compositions that plot at higher Ru/Mo
499 than expected based on the general trend followed by most of the alloys, although none
500 are from *ACM-I*. A simple explanation for these anomalous grains is that they
501 experienced an evaporative event under oxidizing conditions. Fegley and Palme (1985)
502 noted long ago that Mo (and W) are volatile in gases that are oxidizing relative to a gas of
503 solar composition due to stabilization of Mo and W oxides in the vapor. Thus, in Fig. 10,
504 the anomalous alloys may have undergone an evaporative (or condensation) event in a
505 gas that was oxidizing relative to a gas of solar composition. Large depletions (60-90%
506 of expected Mo) are implied. Tungsten concentrations were reported in three of these
507 grains, MUR1 and MUR2 from Croat et al. (2012), and a grain in Allende inclusion 3643
508 described by Wark (1986)]. All three exhibit W depletions. It is perhaps notable that two
509 of the three, MUR1 and MUR2, are included in graphite, which would generally be
510 regarded as an indicator of reducing conditions, and that these are known to be presolar
511 grains (Croat et al. 2012). Molybdenum and W anomalies can also reflect low
512 temperature mobility (e.g., Campbell et al. 2001). If, however, we assume that graphite
513 would have been attacked in an event oxidizing enough to generate the observed Mo and
514 W depletions in MUR1 and MUR2, this suggests that the presolar alloys described by
515 Croat et al. (2012) formed in or were exposed to an oxidizing environment prior to their
516 incorporation in presolar graphite.

517 Notwithstanding the anomalous grains of Fig. 10, most refractory metal grains
518 form a coherent trend in composition, suggesting a common evolution. In the following
519 discussion, we first consider the structures of refractory metal alloys in meteorites. This
520 is important because two phases with identical composition but different structure will
521 have different stabilities as neither the lattice stability nor the solution properties will be

522 the same. We then evaluate the relevant thermodynamic properties and these data are
523 used to calculate alloy compositions for condensation in a cooling gas of solar
524 composition. Through these calculations, we illustrate how hexamolybdenum fits into
525 the broader context of refractory metal alloys in carbonaceous chondrites.

526 Based on INAA analyses of alloy-rich samples, Sylvester et al. (1993) inferred
527 that early condensation of refractory elements involved at least three different carriers.
528 They noted that end-member platinum group elements (PGEs) and Fe-Ni assumed a
529 variety of structural forms and made the testable prediction that the end-members
530 apparent in their data reflected condensation of refractory alloys into phases with three
531 distinct structures. Harries et al. (2012) showed, however, that the PGE-rich alloys in
532 Murchison invariably have a $P6_3/mmc$ structure (our studies of refractory metal nuggets
533 from Allende and a variety of other carbonaceous chondrites (Acfer 094, Murchison,
534 NWA 1934, Vigarano) have also yielded only $P6_3/mmc$ structures) and they, therefore,
535 concluded that Sylvester et al.'s observed groupings were not due to condensation of
536 refractory siderophiles into multiple structures.

537 Berg et al. (2009) calculated alloy compositions as a function of temperature in a
538 cooling gas of solar composition referenced to a total pressure of 10^{-4} bars using
539 procedures and thermodynamic data outlined by Campbell et al. (2001) and oxygen
540 fugacities from Rubin et al. (1988). They then obtained an apparent condensation
541 temperature for an analyzed alloy by finding the one that minimized deviations between
542 calculated and observed alloy compositions. There are two key assumptions in the
543 calculations of Berg et al. (2009): (1) Nonideality in the alloy solution can be neglected
544 and (2) lattice stabilization energies for elements in hexagonal structures are the same as
545 for the corresponding elements in their stable structural state. We briefly consider the
546 effects of these assumptions on calculated alloy compositions.

547 The first assumption is difficult to evaluate in any detail. There are relatively few
548 thermodynamic assessments of binary or higher order systems involving the most
549 refractory elements for Os-Re-Ru-Mo-W-Ir-Pt-Rh alloys. Assessments for Mo-Rh-Ru-
550 Pd-Tc alloys (Kaye et al. 2007) and Mo-W (Gustafson 1988) suggest that activity
551 coefficients, γ_i , in binaries where one element in its pure form has a $P6_3/mmc$ structure
552 (Ru, Tc) with Mo, which has a body center cubic structure, are higher (i.e. more positive)

553 than those involving binary solid solutions of two cubic or two hexagonal structured end-
554 members. For condensates, a higher activity coefficient for an element i in an alloy
555 translates into a lower mole fraction, X_i , because the activity of the element in the
556 condensate, $a_i = \gamma_i X_i$, where γ_i refers to the activity coefficient of element i , is dictated
557 by the vapor pressure of that element in the nebula. Thus, a higher value of γ_i in the alloy
558 translates into a lower value of X_i in a condensate alloy and, conversely, a lower value of
559 γ_i results in a higher than expected value of X_i . Qualitatively, Mo and W will be
560 stabilized in the vapor relative to the alloy by this effect relative to other elements in the
561 alloy. Since we cannot explicitly evaluate γ_i in most of the relevant subsystems for
562 P6₃/mmc alloys, we ignore these effects and use an ideal solution model, following
563 Fegley and Palme (1985) and Berg et al. (2009).

564 The second assumption, that the vapor pressure over hexagonal structured
565 metallic elements is negligibly different from that over the same metal in its stable
566 structural form, can be evaluated quantitatively using available data. Hultgren et al.
567 (1973) tabulated vapor pressures over siderophile elements in their stable structural state
568 as a function of temperature and Campbell et al. (2001) fitted these data to equations of
569 the form

$$\log P_i = -A/T(K) + B \quad (1)$$

570 for interpolation purposes. In equation (1), A and B are empirical coefficients, P_i refers
571 to the vapor pressure of element i over the pure metal, and T is temperature in degrees K.

572 For the refractory elements with stable hexagonal structures at low pressure (Os,
573 Re, or Ru), the expressions of Campbell et al. (2001) are appropriate standard states for
574 hexagonal structured alloys because the stable pure metals for these elements are also
575 hexagonal. For Mo and W, however, the vapor pressures of Hultgren et al. (1973) refer
576 to values over bcc metals and for Ir, Pt, and Rh, they refer to fcc metals. From the lattice
577 stabilization energies given by Dinsdale (1991), fcc Ir, Pt, and Rh are more stable than
578 the hcp metals by 2-3 kJ/mole. For Mo and W, both of which have stable bcc structures
579 in the temperature range of interest, the difference is larger, up to 12 kJ/mole for Mo and
580 15 kJ/mole for W. For temperatures between 1000 and 2000K, these differences translate
581 into vapor pressures over pure metals that are higher than those given in Hultgren et al.
582

583 (1973) by 0.1 - 0.2 *log* units for Ir, Pt, and Rh, 0.3 - 0.6 for Mo, and 0.4 - 0.8 for W, with
584 deviations increasing with decreasing temperature.

585 We used procedures, oxygen fugacities (via Ebel and Grossman 2000), and
586 thermodynamic data outlined by Campbell et al. (2001) to calculate equilibrium alloy
587 condensate compositions but corrected their expressions for elemental vapor pressures
588 over pure metals to values appropriate for hexagonal metals (Table 4). Campbell et al.
589 (2001) specify activity coefficients for some components in the alloy but we set those to
590 one (i.e., we used an ideal solution). Activity coefficients for these alloys are poorly
591 constrained, as noted above, and, moreover, specifying nonideal activity coefficients for a
592 subset of components, while forcing all others to equal one, would violate the Gibbs-
593 Duhem equation. Our computed alloy compositions show that the effect of lattice
594 stabilization is negligible to modest for total pressures of 10^{-4} bar in the temperature
595 range of greatest interest ($\sim 1500 - 1650$ K). Os concentrations can be higher by as much
596 as 0.03 due to destabilization of W, Ir lower by 0.02, and Mo by 0.01. Similar results are
597 obtained if oxygen fugacities of Rubin et al. (1988), which were adopted by Berg et al.
598 (2009), are used.

599 Hexamolybdenum is part of a continuum of $P6_3/mmc$ alloy compositions but the
600 mineral nevertheless provides a useful genetic context. In Fig. 11, we show fields in
601 terms of inverse temperature and total nebular pressure for $P6_3/mmc$ alloy minerals in
602 equilibrium with a cooling gas of solar composition. The plotted lines were calculated
603 assuming an ideal solution for the alloy, using thermodynamic data from Table 4 and
604 Campbell et al. (2001), and employing the calculation procedures of Campbell et al.
605 (2001). Figure 11 may look like a phase diagram but the calculated lines represent
606 conditions for which molar concentrations of the two most abundant elements are equal.
607 This naturally leads to fields within which one element is dominant but, from a
608 thermodynamic perspective, it is important to remember that all of these minerals are the
609 same phase. At any given total pressure, the most refractory meteoritic alloys are
610 osmiums (i.e., Os is the dominant element). With decreasing temperature at a constant
611 pressure, osmium gives way to ruthenium, which is followed by hexamolybdenum and,
612 finally, hexaferrum. In these calculations, Ir is never the dominant element although at
613 least one Ir dominant alloy was observed in *ACM-1* and one might reasonably expect that

614 there is a small field for rutheniridosmine between those of osmium and ruthenium.
615 Stabilization of Ir in the alloy due to nonideality, which is ignored in the calculations,
616 condensation in fractionated nebular gases from which Os has been lost, or kinetic factors
617 may be responsible for the discrepancy. Although not shown, the stability of osmium and
618 hence all P₆₃/mmc alloys is limited at high temperatures by vapor (~1840 K at 10⁻⁴ bar
619 according to Campbell et al. 2001) and at sufficiently high total pressures, by melting.
620 From the perspective of Fig. 11, hexamolybdenum is likely “formed” through the
621 incorporation of enough Mo to semantically “destroy” preexisting ruthenium and is itself
622 semantically “destroyed” through the incorporation of enough Fe to make hexaferrum.
623 Hexamolybdenum and other P₆₃/mmc alloy minerals may also react with gaseous Fe
624 present in the nebula or a parent body, leading to the formation of a cubic ferrous alloy,
625 the dominant form of Fe-rich alloys in chondrites.

626

627

IMPLICATIONS

628 We describe two new minerals, allendeite and hexamolybdenum, from the *ACM-1*
629 ultrarefractory inclusion from the carbonaceous chondrite Allende and, in so doing, open
630 a new window onto processes during the early stages of the formation of the solar system.
631 Both phases are likely high temperature condensates. Allendeite (Sc₃Zr₄O₁₂) is a
632 potentially important indicator of the evolution of refractory lithophile elements.
633 Hexamolybdenum (Mo,Ru,Fe,Ir,Os) is similarly well posed for evaluating the early
634 distribution of refractory siderophiles.

635

636

ACKNOWLEDGEMENTS

637 The Caltech GPS Analytical Facility is supported, in part, by NSF grants EAR-
638 0318518 and DMR-0080065. We also acknowledge NASA grant NNX12AH63G and
639 NSF EAR-0947956. We thank the Smithsonian Institution for additional Allende samples
640 and Dr. H.C. Connolly, Jr. for bringing them to our attention. The review of A.M. Davis
641 led to significant improvements in the manuscript.

642

643

644

REFERENCES

- 645 Anderson, E. and Hume-Rothery, W. (1960) The equilibrium diagram of the system
646 Molybdenum-Ruthenium. *Journal of the Less-Common Metals*, 2, 443–450.
- 647 Armstrong, J.T. (1995) CITZAF - a package of correction programs for the quantitative
648 electron microbeam X-ray-analysis of thick polished materials, thin-films, and
649 particles. *Microbeam Analysis*, 4, 177–200.
- 650 Belov, A.N., Semenov, G.A., Teterin, G.A., and Shkol'nikova, T.M. (1987) Evaporation
651 and thermodynamic properties of Sc_2O_3 and of $\text{ZrO}_2\text{-Sc}_2\text{O}_3$ binary solid solutions
652 according to high-temperature mass spectrometry data. II. Calculations. *Russian*
653 *Journal of Physical Chemistry*, 61, 468–470.
- 654 Berg, T., Maul, J., Schönhense, G., Marosits, E., Hoppe, P., Ott, U., and Palme, H. (2009)
655 Direct evidence for condensation in the early solar system and implications for
656 nebular cooling rates. *Astrophysical Journal*, 702, L172–L176.
- 657 Blander, M., Fuchs, L.H., Horowitz, C., and land, R. (1980) Primordial refractory metal
658 particles in the Allende meteorite. *Geochimica et Cosmochimica Acta*, 44, 217–223.
- 659 Blum, J.D., Wasserburg, G.J., Hutcheon, I.D., Beckett, J.R., and Stolper, E.M. (1989)
660 Origin of opaque assemblages in C3V meteorites: Implications for nebular and
661 planetary processes. *Geochimica et Cosmochimica Acta*, 53, 543–556.
- 662 Bogatikov, O.A., Gorshkov, A.I., Mokhov, A.V., Ashikhmina, N.A., and Magazina, L.O.
663 (2001) The first finding of native molybdenum, silver sulfide, and iron-tin alloy in
664 the lunar regolith. *Geochemistry International*, 39, 604–608.
- 665 Bogatikov, O.A., Mokhov, A.V., Gorshkov, A.I., Ashikhmina, N.A., Magazina, L.O.,
666 Kartashov, P.M., and Koporulina, E.V. (2002) High-quality gold, Cu-Zn-Au-Ag
667 solid solution, and native Mo in the AS Luna 16 regolith. *Doklady Earth Sciences*,
668 386, 827–830.
- 669 Campbell, A.J., Humayun, M., Meibom, A., Krot, A.N., and Keil, K. (2001) Origin of
670 zoned metal grains in the QUE94411 chondrite. *Geochimica et Cosmochimica Acta*,
671 65, 163–180.
- 672 Clarke, R.S., Jarosewich, E., Mason, B., Nelen, J., Gómez, M., and Hyde, J.R. (1970)
673 The Allende, Mexico, meteorite shower. *Smithsonian Contributions to the Earth*
674 *Sciences*, 5, 1–53

- 675 Croat, T.K., Berg, T., Jadhav, M., and Bernatowicz, T.J. (2012) Presolar refractory metal
676 nuggets. Lunar and Planetary Science Conference, 43, Abstract #1503.
- 677 Dinsdale, A.T. (1991) SGTE data for pure elements. CALPHAD, 15, 317–425.
- 678 Ebel, D.S. and Grossman, L. (2000) Condensation in dust-enriched systems. *Geochimica*
679 *et Cosmochimica Acta*, 64, 339–366.
- 680 El Goresy, A., Nagel, K, and Ramdohr, P. (1978) Fremdlinge and their noble relatives.
681 *Proceedings of the Lunar and Planetary Science Conference*, 9, 1279–1303.
- 682 El Goresy, A., Zinner, E., Matsunami, S., Palme, H., Spettel, B., Lin, Y., and Nazarov, M.
683 (2002) Efremovka 101.1: A CAI with ultrarefractory REE patterns and enormous
684 enrichments of Sc, Zr, and Y in fassaite and perovskite. *Geochimica et*
685 *Cosmochimica Acta*, 66, 1459–1491.
- 686 Fegley, B. and Palme, H. (1985) Evidence for oxidizing conditions in the solar nebula
687 from Mo and W depletions in refractory inclusions in carbonaceous chondrites.
688 *Earth and Planetary Science Letters*, 72, 311–326.
- 689 Fleischer, M. (1970) New mineral names. *American Mineralogist*, 55, 317-323.
- 690 Fuchs, L. (1969) Occurrence of cordierite and aluminous orthoenstatite in the Allende
691 meteorite. *American Mineralogist*, 54, 1645–1653.
- 692 Fuchs, L. (1971) Occurrence of wollastonite, rhönite, and andradite in the Allende
693 meteorite. *American Mineralogist*, 56, 2053–2068.
- 694 Fuchs, L. and Blander, M. (1977) Molybdenite in calcium-aluminum-rich inclusions in
695 the Allende meteorite. *Geochimica et Cosmochimica Acta*, 41, 1170–1175.
- 696 Gaft, M., Reisfeld, R., and Panczer, G. (2005) *Modern Luminescence Spectroscopy of*
697 *Minerals and Materials*. Springer-Verlag, Berlin. Chapter 4.
- 698 Grossman, L. (1973) Refractory trace elements in Ca-Al-rich inclusions in the Allende
699 meteorite. *Geochimica et Cosmochimica Acta*, 37, 1119–1140.
- 700 Gustafson, P. (1988) An experimental study and a thermodynamic evaluation of the Fe-
701 Mo-W system. *Zeitschrift für Metallkunde*, 79, 388–396.
- 702 Harries, D., Berg, T., Langenhorst, F., and Palme, H. (2012) Structural clues to the origin
703 of refractory metal alloys as condensates of the solar nebula. *Meteoritics &*
704 *Planetary Science*, 47, 2148–2159.

- 705 Hinton, R.W., Davis, A.M., Scatena-Wachel, D.E., Grossman, L., and Draus, R.J. (1988)
706 A chemical and isotopic study of hibonite-rich refractory inclusions in primitive
707 meteorites. *Geochimica et Cosmochimica Acta*, 52, 2573–2598.
- 708 Hultgren, R., Desai, P.D., Hawkins, D.T., Gleizer, M., Kelley, K.K., and Wagman, D.D.
709 (1973) Selected Values of the Thermodynamic Properties of the Elements.
710 American Society for Metals.
- 711 Ireland, T.R., Fahey, A.J., and Zinner, E.K. (1988) Trace-element abundances in hibonite
712 from the Murchison carbonaceous chondrite: Constraints on high-temperature
713 processes in the solar nebula. *Geochimica et Cosmochimica Acta*, 52, 2841–2854.
- 714 Ireland, T.R., Fahey, A.J., and Zinner, E.K. (1991) Hibonite-bearing microspherules: a
715 new type of refractory inclusion. *Geochimica et Cosmochimica Acta*, 55, 367–379.
- 716 Jacobson, N.S., Copland, E.H., and Kaufman, L. (2001) Thermodynamic database for the
717 $\text{NdO}_{1.5}\text{-YO}_{1.5}\text{-YbO}_{1.5}\text{-ScO}_{1.5}\text{-ZrO}_2$ system. Nasa Technical Memorandum 2001-
718 210753, 44 pp.
- 719 Kaye, M.H., Lewis, B.J., and Thompson, W.T. (2007) Thermodynamic treatment of
720 noble metal fission products in nuclear fuel. *Journal of Nuclear Materials*, 366, 8–27.
- 721 Keil, K. and Fuchs, L.H. (1971) Hibonite $[\text{Ca}_2(\text{Al,Ti})_{24}\text{O}_{38}]$ from the Leoville and
722 Allende chondritic meteorites. *Earth and Planetary Science Letters*. 12, 184–190.
- 723 Keller, L.P. and Buseck, P. (1989) Alteration of Ca- and Al-rich inclusions in Allende: A
724 transmission electron microscope study. *Lunar and Planetary Science*, 20,
725 512–513.
- 726 Kerridge, J.F. and Matthews, M.S. (1988) *Meteorites and the Early Solar System*.
727 University of Arizona Press, 1269 pp.
- 728 Kleykamp, H. (1988) The constitution of the Mo-Ru system. *Journal of the Less-*
729 *Common Metals*, 136, 271–275.
- 730 Konev, A.A., Ushchapovskaya, Z.F., Kashaev, A.A., and Lebedeva, V.S. (1969)
731 Tazheranite, a new calcium-titanium-zirconium mineral. *Doklady Academia*
732 *Nauk SSSR*, 186, 917–920 (in Russian).
- 733 Kornacki A.S. and Fegley, B. (1986) The abundance and relative volatility of refractory
734 trace elements in Allende Ca,Al-rich inclusions: implications for chemical and

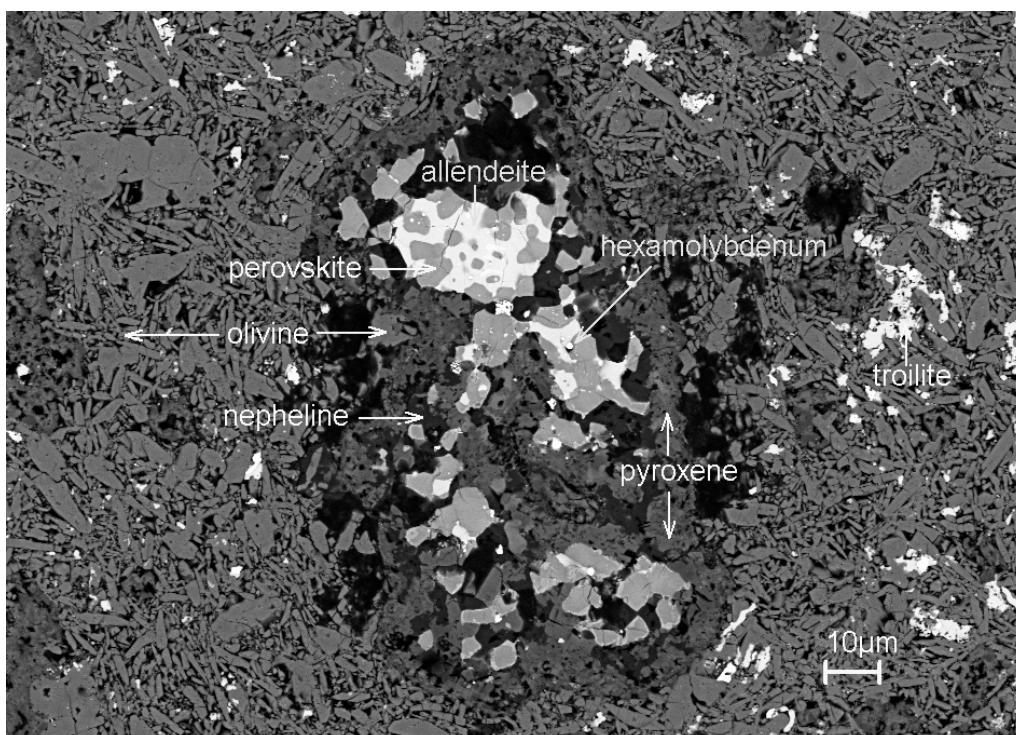
- 735 physical processes in the solar nebula. *Earth and Planetary Science Letters*, 79,
736 217–234.
- 737 Kraus, W. and Nolze, G. (1996) POWDER CELL – a program for the representation and
738 manipulation of crystal structures and calculation of the resulting X-ray powder
739 patterns. *Journal of Applied Crystallography*, 29, 301–303.
- 740 Lauretta, D.S. and McSween, H.Y. (2006) *Meteorites and the Early Solar System*.
741 University of Arizona Press, 943 pp.
- 742 Lin, Y., El Goresy, A., and Ouyang, Z. (1999) Ca-, Al-rich refractory inclusions and Pt-
743 metal nuggets in the Ningqiang carbonaceous chondrite. *Chinese Science Bulletin*,
744 44, 725–731.
- 745 Lodders, K. (2003) Solar system abundances and condensation temperatures of the
746 elements. *Astrophysical Journal*, 591, 1220–1247.
- 747 Lovering, J.F., Wark, D.A., and Sewell, D.K.B. (1979) Refractory oxide, titanite, niobate
748 and silicate accessory mineralogy of some type B Ca-Al-rich inclusions in the
749 Allende meteorite. *Lunar and Planetary Science*, 10, 745–746.
- 750 Ma, C. (2010) Hibonite-(Fe), (Fe,Mg)Al₁₂O₁₉, a new alteration mineral from the Allende
751 meteorite. *American Mineralogist*, 95, 188–191.
- 752 Ma, C. (2011) Discovery of meteoritic lakargiite (CaZrO₃), a new ultra-refractory mineral
753 from the Acfer 094 carbonaceous chondrite. *Meteoritics & Planetary Science*, 46
754 (S1), A144.
- 755 Ma, C. (2012) Discovery of meteoritic eringaite, Ca₃(Sc,Y,Ti)₂Si₃O₁₂, the first solar
756 garnet. *Meteoritics & Planetary Science*, 47 (S1), A256.
- 757 Ma, C. (2013a) Majindeite, IMA 2012-079. CNMNC Newsletter No. 15, February 2013,
758 page 10. *Mineralogical Magazine*, 77, 1–12.
- 759 Ma, C. (2013b) Nuwaite, IMA 2013-018. CNMNC Newsletter No. 16, August 2013,
760 page 2704. *Mineralogical Magazine*, 77, 2695–2709.
- 761 Ma, C. and Krot, A.N. (2013) Discovery of a new garnet mineral, Ca₃Ti₂(SiAl₂)O₁₂: An
762 alteration phase in Allende. *Meteoritics & Planetary Science*, 48 (S1), Abstract
763 5049.
- 764 Ma, C. and Rossman, G.R. (2008a) Barioperovskite, BaTiO₃, a new mineral from the
765 Benitoite Mine, California. *American Mineralogist*, 93, 154–157.

- 766 Ma, C. and Rossman, G.R. (2008b) Discovery of tazheranite (cubic zirconia) in the
767 Allende meteorite. *Geochimica et Cosmochimica Acta*, 72, A577.
- 768 Ma, C. and Rossman, G.R. (2009a) Tistarite, Ti_2O_3 , a new refractory mineral from the
769 Allende meteorite. *American Mineralogist*, 94, 841–844.
- 770 Ma, C. and Rossman, G.R. (2009b) Davisite, $CaScAlSiO_6$, a new pyroxene from the
771 Allende meteorite. *American Mineralogist*, 94, 845–848.
- 772 Ma, C. and Rossman, G.R. (2009c) Grossmanite, $CaTi^{3+}AlSiO_6$, a new pyroxene from
773 the Allende meteorite. *American Mineralogist*, 94, 1491–1494.
- 774 Ma, C., Beckett, J.R., and Rossman, G.R. (2009a) Allendeite and hexamolybdenum: Two
775 new ultra-refractory minerals in Allende and two missing links. *Lunar and Planetary*
776 *Science Conference*, 40, Abstract # 1402.
- 777 Ma, C., Beckett, J.R., Rossman, G.R., Connolly, H.C., Guan, Y., Eiler, J.M., and
778 Hofmann, A.E. (2009b) In-situ discovery of a cluster of refractory grains in an
779 Allende ferromagnesian chondrule. *Lunar and Planetary Science Conference*, 40,
780 Abstract # 2138.
- 781 Ma, C., Kampf, A.R., Connolly, Jr H.C., Beckett, J.R., Rossman, G.R., Sweeney Smith,
782 S.A., and Schrader, D.L. (2011) Krotite, $CaAl_2O_4$, a new refractory mineral from the
783 NWA 1934 meteorite. *American Mineralogist*, 96, 709–715.
- 784 Ma, C., Tschauer, O., Beckett, J.R., Rossman, G.R., and Liu, W. (2012) Panguite,
785 $(Ti^{4+}, Sc, Al, Mg, Zr, Ca)_{1.8}O_3$, a new ultra-refractory titania mineral from the Allende
786 meteorite: Synchrotron micro-diffraction and EBSD. *American Mineralogist*, 97,
787 1219–1225.
- 788 Ma, C., Beckett, J.R., and Rossman, G.R. (2013a) Discovery of meteoritic lovingite,
789 $Ca(Ti, Fe, Cr, Mg)_{21}O_{38}$, in an Allende chondrule: Late-stage crystallization from a
790 melt droplet. *Lunar and Planetary Science Conference*, 44, Abstract # 1443.
- 791 Ma, C., Krot, A.N., and Bizzarro, M. (2013b) Discovery of dmisteinbergite (hexagonal
792 $CaAl_2Si_2O_8$) in the Allende meteorite: A new member of refractory silicates formed
793 in the solar nebula. *American Mineralogist*, 98, 1368–1371.
- 794 Ma, C., Tschauer, O., Beckett, J.R., Rossman, G.R., and Liu, W. (2013c) Kangite,
795 $(Sc, Ti, Al, Zr, Mg, Ca, \square)_2O_3$, a new ultrarefractory scandia mineral from the Allende

- 796 meteorite: Synchrotron micro-Laue diffraction and electron backscatter diffraction.
797 American Mineralogist, 98, 870–878.
- 798 Ma, C., Beckett, J.R., and Rossman, G.R. (2014) Monipite, MoNiP, a new phosphide
799 mineral in a Ca-Al-rich inclusion from the Allende meteorite. American
800 Mineralogist, 99, in press.
- 801 Michel, D., Perez y Jorba, M., and Collongues, R. (1976) Study by Raman spectroscopy
802 of order-disorder phenomena occurring in some binary oxides with fluorite-related
803 structures. Journal of Raman Spectroscopy, 5, 163–80.
- 804 Noonan, A.F., Nelen, J., Fredriksson, K., and Newbury, D. (1977) Zr-Y oxides and high-
805 alkali glass in an amoeboid inclusion from Ornans. Meteoritics, 12, 332–334.
- 806 Paque, J.M. (1989) Vanadium-rich refractory platinum metal nuggets from a fluffy Type
807 A inclusion in Allende. Lunar and Planetary Science, 20, 822–823.
- 808 Paque J.M., Beckett, J.R., and Burnett, D.S. (2008) Refractory metal nugget as an
809 indicator of alteration processes in a V-rich Ca-Al-rich inclusion. Lunar and
810 Planetary Science, 39, Abstract #1841.
- 811 Park, Y.J., Lee, J.-G., Jee, K.Y., Huh, D.Y., and Kim, W.H. (2000) Structural analysis of
812 simulated fission-produced noble metal alloys and their superconductivities.
813 Bulletin of the Korean Chemical Society, 21, 1187–1192.
- 814 Pawar, R.R. (1967) Lattice expansion of molybdenum. High Temperatures-High
815 Pressures, 7, 221–226.
- 816 Pouchou, J.-L. and Pichoir, F. (1991) Quantitative analysis of homogeneous or stratified
817 microvolumes applying the model "PAP". In Electron Probe Quantitation (Heinrich,
818 K.F.J. and Newbury, D.E., eds.), Plenum Press, 31–75.
- 819 Raub, E. (1954) Die Legierung der Platinmetalle mit Molybdaen. Zeitschrift fuer
820 Metallkunde, 45, 23–30.
- 821 Red'ko, V.P. and Lopato, L.M. (1991) Crystal structure of rare earth zirconates $M_4Zr_3O_{12}$
822 and hafnates $M_4Hf_3O_{12}$ (M = rare earth). Izvestiya Akademii Nauk SSSR,
823 Neorganicheskie Materialy, 27, 1905–1910 (in Russian).
- 824 Richter, F.M., Mendybaev, R.A., and Davis, A.M. (2006) Conditions in the
825 protoplanetary disk as seen by the type B CAIs. Meteoritics & Planetary Science,
826 41, 83–93.

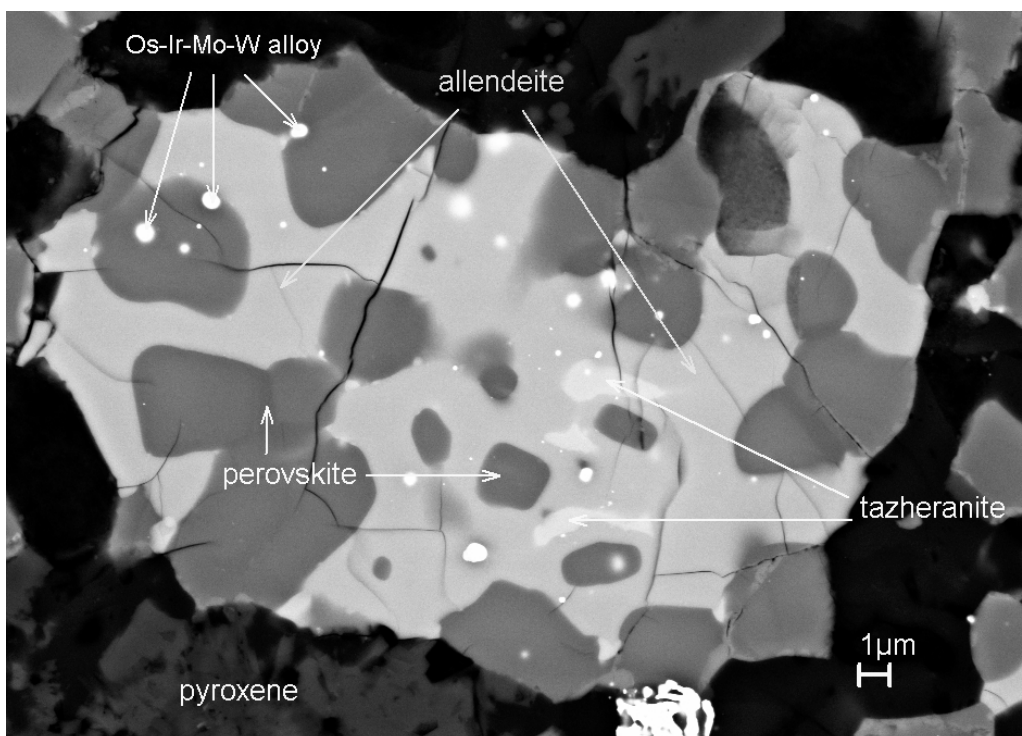
- 827 Robie, R.A., Hemingway, B.S., and Fisher, J.R. (1979) Thermodynamic properties of
828 minerals and related substances at 298.15 K and 1 bar (10^5 Pascals) pressure and at
829 higher temperatures. U.S. Geological Survey Bulletin, 1452, 1–456.
- 830 Rossell, H.J. (1976) Crystal structures of some fluorite-related M_7O_{12} compounds.
831 Journal of Solid State Chemistry, 19, 103-111.
- 832 Rubin, A.E. (1997) Mineralogy of meteorite groups. Meteoritics & Planetary Science,
833 32, 231–247.
- 834 Rubin, A.E., Fegley, B., and Brett, R. (1988) Oxidation state in chondrites. In Meteorites
835 and the Early Solar System (J.F. Kerridge and M.S. Matthews, eds.), University of
836 Arizona Press, 488–511.
- 837 Sahijpal S., Marhas, K.K., and Goswami, J.N. (2003) Determination of rare earth and
838 refractory trace element abundances in early solar system objects by ion microprobe.
839 Proceedings of the Indian Academy of Sciences, 112, 485–498.
- 840 Simon, S.B., Grossman, L., and Davis, A.M. (1991) Fassaite composition trends during
841 crystallization of Allende Type B refractory inclusion melts. Geochimica et
842 Cosmochimica Acta, 55, 2635–2655.
- 843 Simon, S.B., Davis, A.M., and Grossman, L. (1999) Origin of compact type A refractory
844 inclusions from CV3 carbonaceous chondrites. Geochimica et Cosmochimica Acta
845 63, 1233–1248.
- 846 Simon, S.B., Davis, A.M., Grossman, L., and McKeegan, K.D. (2002) A hibonite-
847 corundum inclusion from Murchison: A first generation condensate from the solar
848 nebula. Meteoritics & Planetary Science, 37, 533–548.
- 849 Stolper, E. and Paque, J. M. (1986) Crystallization sequences of Ca-Al-rich inclusions
850 from Allende - The effects of cooling rate and maximum temperature. Geochimica et
851 Cosmochimica Acta, 50, 1785–1806.
- 852 Sylvester, P.J., Simon, S.B., and Grossman, L. (1993) Refractory inclusions from teh
853 Leoville, Efremovka, and Vigarano C3V chondrites: Major element differences
854 between Types A and B, and extraordinary refractory siderophile element
855 compositions. Geochimica et Cosmochimica Acta, 57, 3763–3784.

- 856 Thornber, M.R., Bevan, D.J.M., and Graham, J. (1968) Mixed oxides of the type MO_2
857 (fluorite) – M_2O_3 . III. Crystal structures of the intermediate phases $\text{Zr}_5\text{Sc}_2\text{O}_{13}$ and
858 $\text{Zr}_3\text{Sc}_4\text{O}_{12}$. *Acta Crystallographica*, B24, 1183–1190.
- 859 Urashima, Y., Wakabayashi, T., Masaki, T., and Teresaki, Y. (1974) Ruthenium, a new
860 mineral from Horokanai, Hokkaido, Japan. *Mineralogical Journal*, 7, 438–444.
- 861 Wark, D.A. (1986) Evidence for successive episodes of condensation at high temperature
862 in a part of the solar nebula. *Earth and Planetary Science Letters*, 77, 129–148.
- 863 Wark, D.A. and Lovering, J.F. (1976) Refractory/platinum metal grains in Allende
864 Calcium-aluminum-rich clasts (CARC's): possible exotic solar material. *Lunar and*
865 *Planetary Science*, 7, 912–914.
- 866 Weber, D. and Bischoff, A. (1994) The occurrence of grossite (CaAl_4O_7) in chondrites.
867 *Geochimica et Cosmochimica Acta*, 58, 3855–3877.
- 868



869
870
871
872

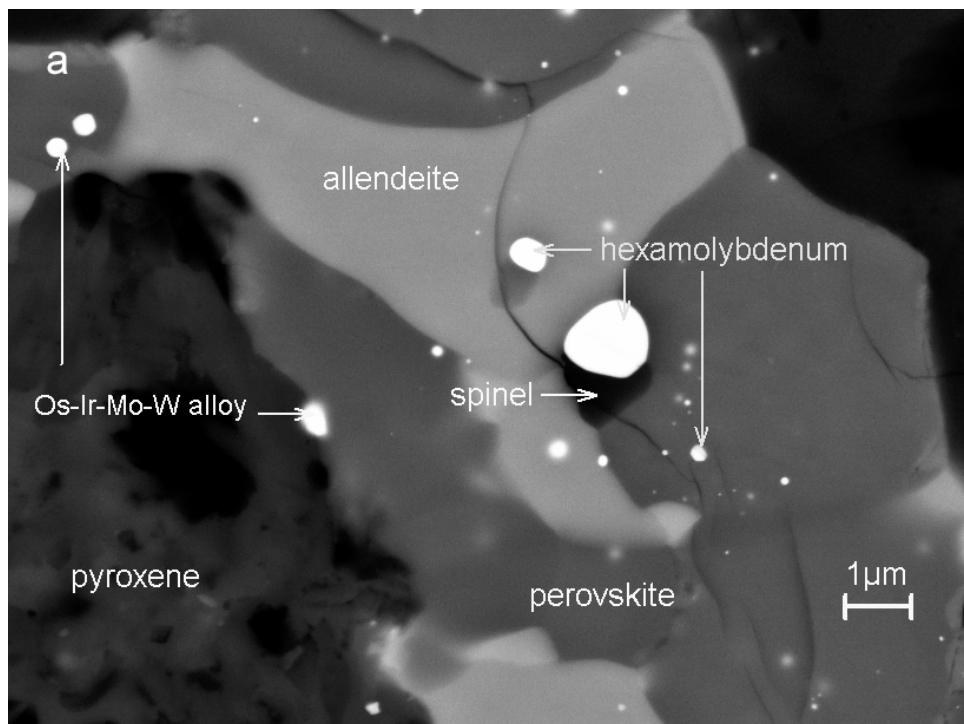
Fig. 1. Backscattered electron (BSE) image of the ultrarefractory inclusion *ACM-1* containing allendeite and hexamolybdenum in polished Allende section USNM 7554.



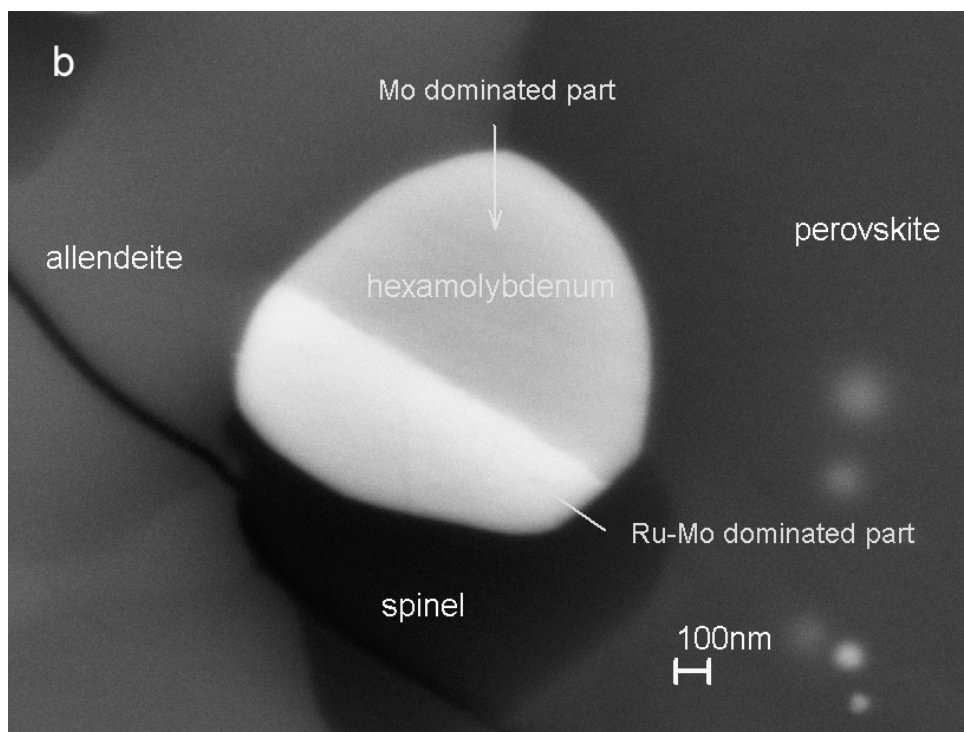
873
874
875
876
877

Fig. 2. Enlarged BSE image showing a single crystal of allendeite (cf. Fig. 1) with included perovskite, tazheranite, and Os-, Ir-, Mo-, W-rich alloys.

878
879



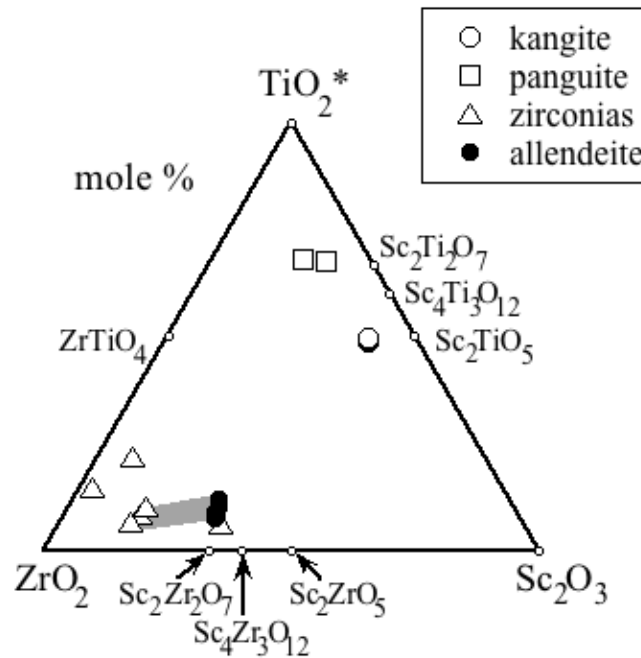
880
881



882
883
884
885
886
887

Fig. 3. BSE images showing a portion of *ACM-1* (cf. Fig. 1). (a) Region containing hexamolybdenum, allendeite, perovskite, and Os-Ir-Mo-W alloys. (b) Enlarged BSE image showing the hexamolybdenum crystal (1.2 μm across).

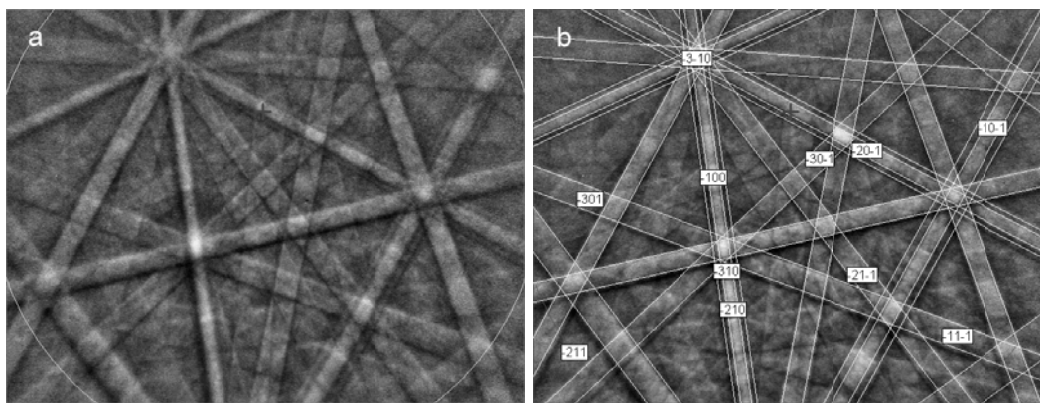
888



889

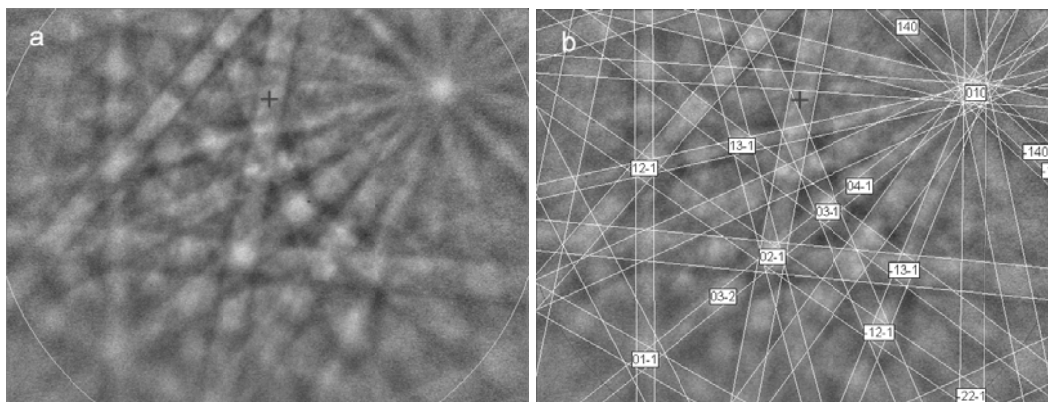
890

891 Fig. 4. Compositions (mole %) of Zr- and Sc-enriched oxides in carbonaceous chondrites
892 in terms of the ternary Sc_2O_3 - TiO_2^* - ZrO_2 , where TiO_2^* represents all Ti calculated as
893 TiO_2 . Coexisting allendeite and tazheranite from *ACM-1* are connected by a gray tie line.
894 Known synthetic compounds within the system Sc_2O_3 - TiO_2 - ZrO_2 are plotted as small
895 small circles. The “zirconia” that plots near the allendeite from this study is described by
896 Weber and Bischoff (1994). The structure of this phase is not known but, based on
897 composition, it is likely to be an allendeite. Data for meteoritic phases are taken from
898 Noonan et al. (1977), Lovering et al. (1979), Hinton et al. (1988), Weber and Bischoff
899 (1994), Ma and Rossman (2008b), Ma et al. (2012, 2013c), and this study.
900



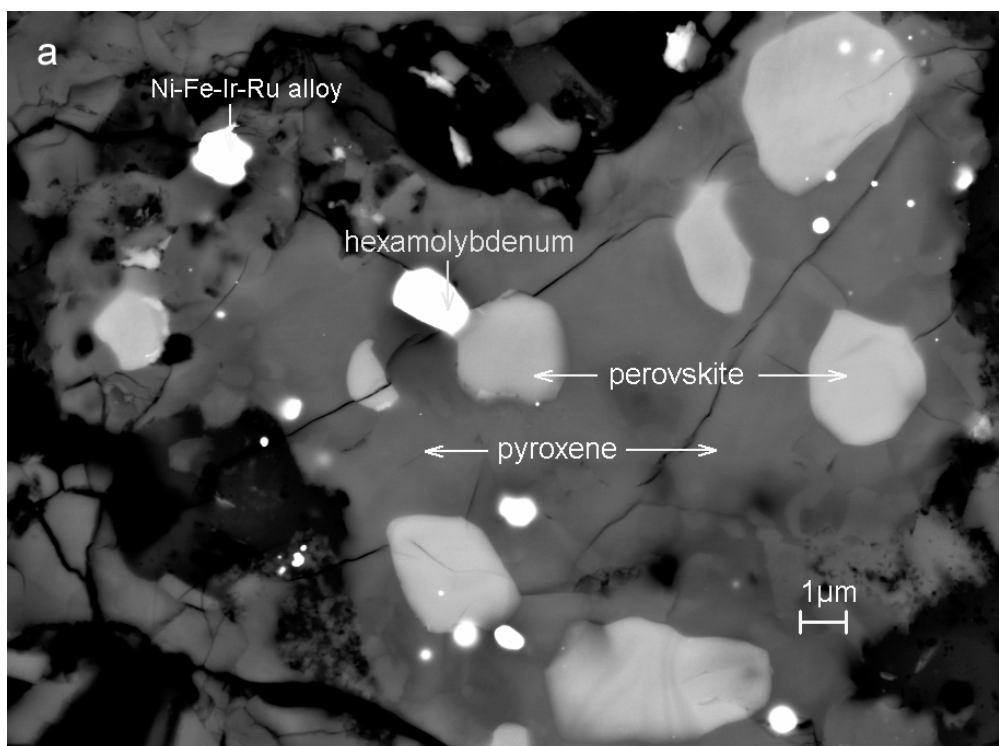
902
903
907
908
909
910
908
909
910

Fig. 5. (a) EBSD pattern of the allendeite crystal shown in Fig. 2. The blue cross indicates the center of the EBSD pattern. Portions of a green circle are also shown. This circle encloses the EBSD area used for defining the diffracting bands. (b) The EBSD pattern shown in panel (a) indexed using the $\text{Sc}_4\text{Zr}_3\text{O}_{12}$ $R\bar{3}$ structure as given by Rossell (1976).

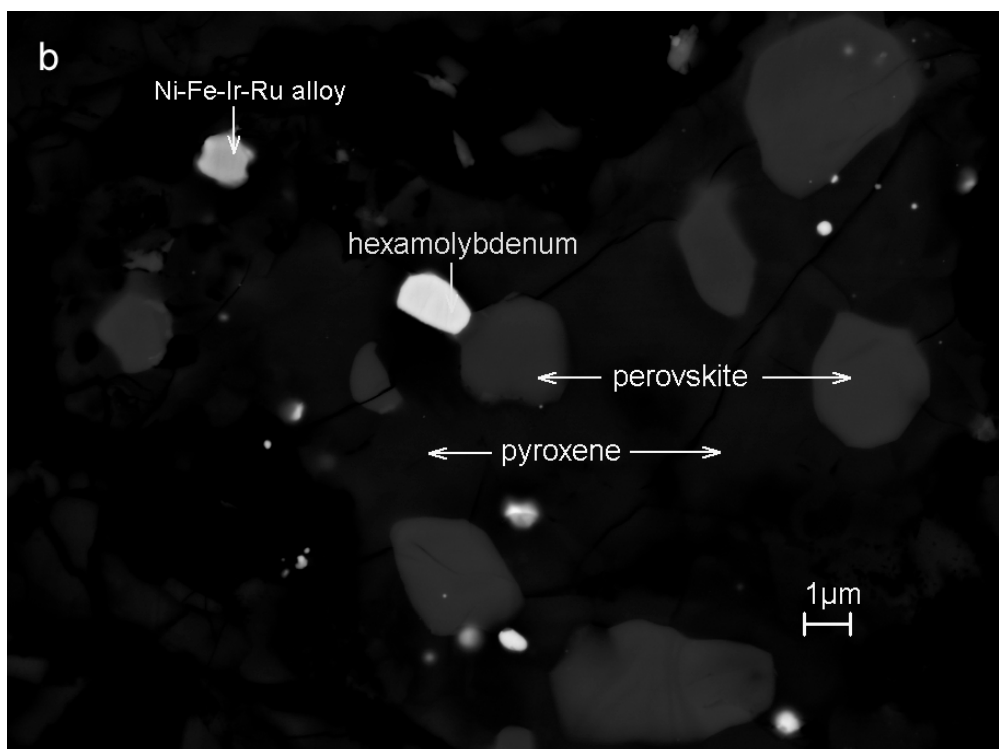


911
912
916
917
918
919
917
918

Fig. 6. (a) EBSD pattern of the 1.2 μm hexamolybdenum from *ACM-1* (Fig. 3). The green circle and blue cross have the same meaning as in Fig. 5. (b) the pattern is best indexed using the $P6_3/mmc$ structure of the synthetic $\text{Mo}_{55}\text{Ru}_{45}$ phase described by Anderson and Hume-Rothery (1960).



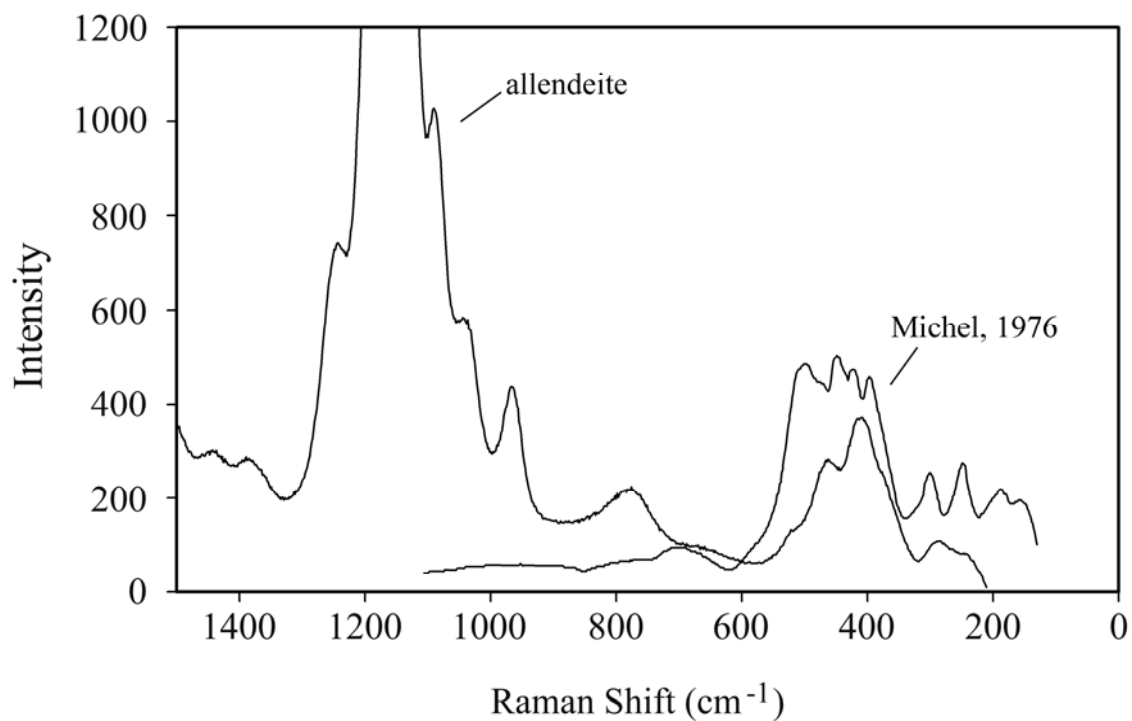
918
919



920
921
922
923
924
925

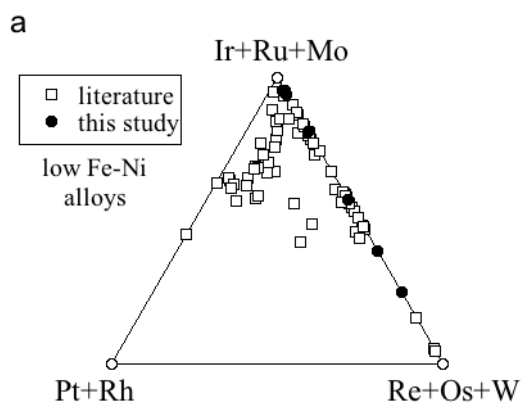
Fig. 7. BSE images showing one hexamolybdenum grain in a fine-grained inclusion from USNM polished thin section 3509HC12 with contrast optimized for (a) silicates and oxides and (b) alloys. Note the difference in Z contrast between hexamolybdenum and the Ni-Fe-Ir-Ru alloy in the upper left of the panel.

926
927

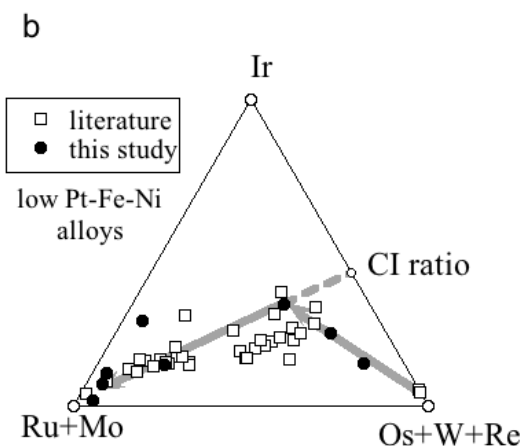


928
929
930
931
932
933
934
935

Fig. 8. Raman spectrum of allendeite (this study), which has intense bands in the 1300-1000 cm⁻¹ region, and synthetic Sc₄Zr₃O₁₂ (Michel et al. 1976), which shows no evidence for features in this region of the spectrum.



936



937

938

939

940

941

942

943

944

945

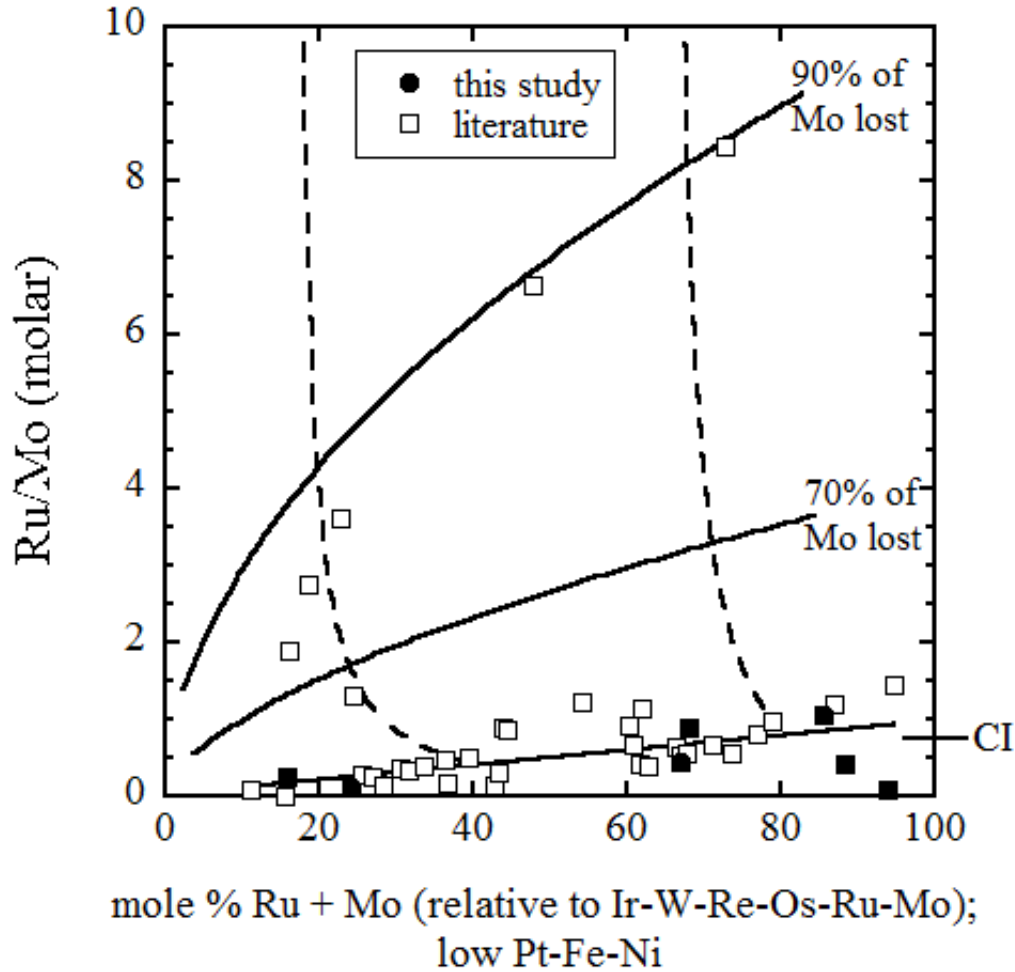
946

947

948

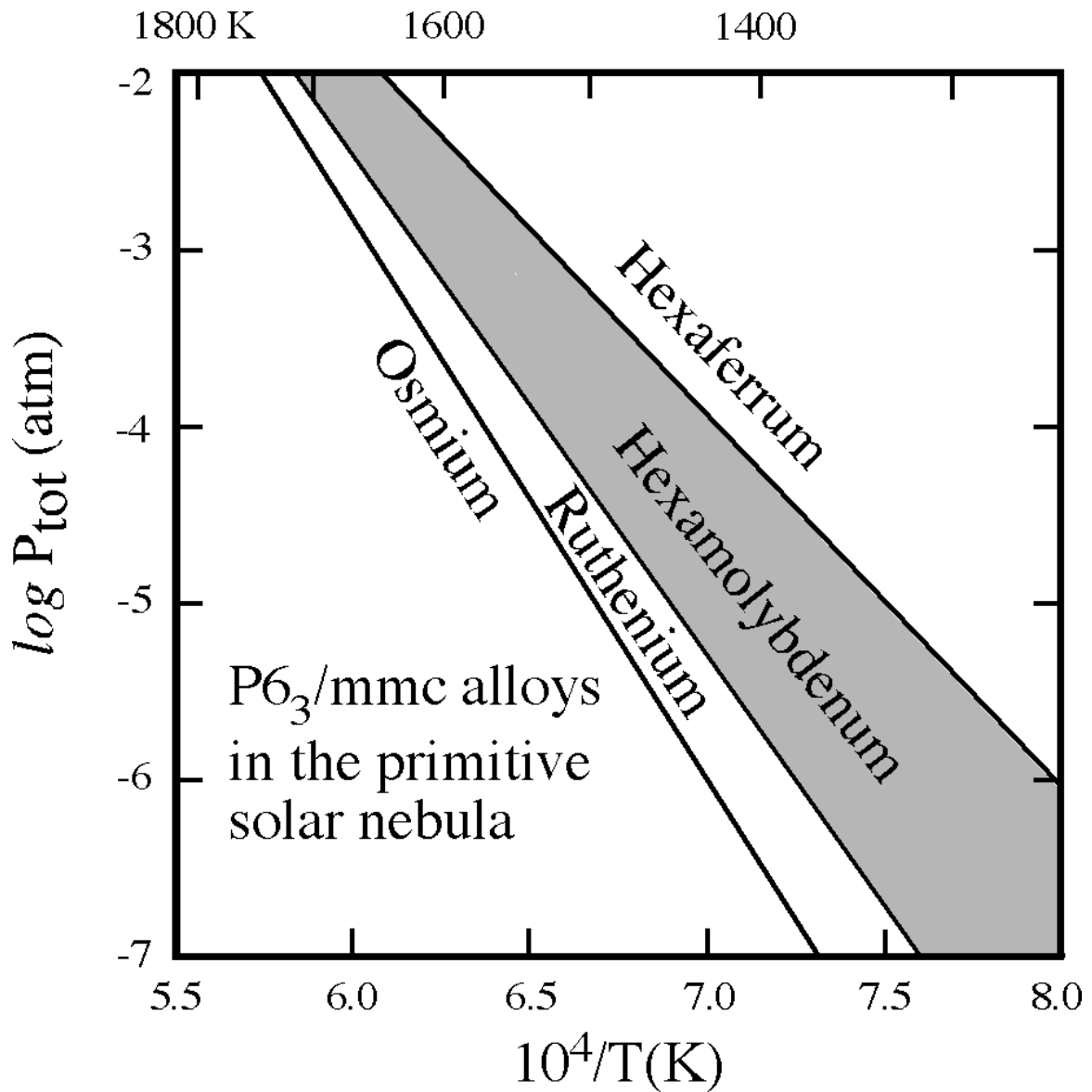
Fig. 9. Refractory alloy compositions in chondrites (molar basis). Alloys high in the more volatile elements Fe, Ni and V (sum of mole fractions > 0.4) were excluded. Data were taken from Wark and Lovering (1976), Blander et al. (1980), Wark (1986), Lin et al. (1999), Berg et al. (2009), Harries et al. (2012), Croat et al. (2012), Ma (2011), and this study. (a) The ternary (Re+Os+W) - (Ir+Ru+Mo) - (Pt+Rh). Alloys from this study have low concentrations of the moderately volatile PGEs Pt and Rh. (b) (Re+Os+W) - (Ir) - (Ru+Mo). Gray lines indicate direction of increasing volatility (lower relative temperature of condensation).

949



950
951
952
953
954
955
956
957
958
959

Fig. 10. Ru + Mo expressed as mole % of the refractory alloy elements that are at least as refractory as Ru and Mo as a function of the molar Ru/Mo ratio. An unweighted regression line is drawn through the data, excluding the six points plotting furthest from the general trend. Dashed curves terminate at the regression line and extend upward through progressive loss of Mo. Solid curves describe the locus of points for specific amounts of the original Mo removed. Data sources as in Fig. 9.



960
961
962
963
964
965

Fig. 11. Calculated fields for condensate $P6_3/mmc$ mineral alloys in a cooling gas of solar composition. The field for hexamolybdenum is shaded. Lines represent the loci of points for which the two elements with the highest concentrations in the condensate alloy are equal.

Table 1: Oxides and silicates in allendeite- and hexamolybdenum-bearing phase assemblages

Phase	allendeite	perovskite	tazheranite	Mg-Al spinel	Fe-Al spinel	sodalite	nepheline	Al-rich, low-Ti augite	perovskite ^a	pyroxene ^a
Section	USNM 7554	USNM 7554	USNM 7554	USNM 7554	USNM 7554	USNM 7554	USNM 7554	USNM 7554	USNM 3509HC12	USNM 3509HC12
type	EPMA ^b	EPMA	EPMA	SEM-EDS ^c	SEM-EDS	SEM-EDS	SEM-EDS	SEM-EDS	SEM-EDS	SEM-EDS
# analyses	8	7	2	1	1	1	1	1	1	1
Na ₂ O	n.d. ^d	n.d.	n.d.	n.d.	n.d.	17.99 (0.46)	12.67 (0.50)	n.d.	n.d.	n.d.
MgO	n.d.	n.d.	n.d.	11.64 (0.20) ^c	12.14 (0.35)	0.91 (0.23)	1.97 (0.33)	4.48 (0.22)	n.d.	2.73 (0.13)
Al ₂ O ₃	0.70 (0.03) ^b	1.26 (0.17)	0.45 (0.04)	33.44 (0.34)	61.28 (0.68)	28.38 (0.64)	29.77 (0.77)	15.80 (0.34)	3.09 (0.17)	27.72 (0.28)
SiO ₂	n.d.	n.d.	n.d.	n.d.	1.69 (0.28)	39.24 (0.81)	46.41 (1.07)	42.85(0.53)	n.d.	20.90 (0.28)
Cl	n.d.	n.d.	n.d.	n.d.	n.d.	7.37 (0.29)	n.d.	n.d.	n.d.	n.d.
K ₂ O	n.d.	n.d.	n.d.	n.d.	n.d.	n.d.	1.63 (0.25)	n.d.	n.d.	n.d.
CaO	2.74 (0.50)	34.26 (1.05)	6.52 (1.07)	17.38 (0.24)	0.63 (0.15)	0.94 (0.24)	2.79 (0.34)	27.67 (0.39)	35.00 (0.39)	22.59 (0.25)
Sc ₂ O ₃	32.36 (0.51)	2.50 (1.20)	15.23 (1.06)	2.77 (0.20)	n.d.	n.d.	n.d.	n.d.	n.d.	6.72 (0.23)
TiO ₂	5.47 (0.89)	48.01 (1.47)	4.84 (1.33)	26.39 (0.37)	n.d.	2.45 (0.43)	n.d.	n.d.	51.70 (0.57)	11.93 (0.28)
V ₂ O ₃	0.35 (0.04)	0.41 (0.08)	0.23 (0.00)	1.16 (0.22)	n.d.	n.d.	n.d.	n.d.	n.d.	1.15 (0.19)
Cr ₂ O ₃	0.02 (0.03)	0.06 (0.03)	0.02 (0.01)	n.d.	n.d.	n.d.	n.d.	n.d.	n.d.	n.d.
FeO ^{*e}	0.82 (0.04)	0.70 (0.04)	0.87 (0.06)	1.52 (0.22)	24.25 (0.62)	2.73 (0.75)	4.76 (1.04)	9.20 (0.46)	0.87 (0.25)	0.99 (0.19)
Y ₂ O ₃	0.70 (0.07)	3.84 (0.97)	2.12 (0.22)	n.d.	n.d.	n.d.	n.d.	n.d.	7.17 (0.46)	n.d.
ZrO ₂	56.58 (1.20)	7.87 (2.29)	68.42 (3.11)	5.70 (0.42)	n.d.	n.d.	n.d.	n.d.	2.17 (0.46)	5.27 (0.34)
HfO ₂	1.21 (0.15)	0.14 (0.14)	1.34 (0.10)	n.d.	n.d.	n.d.	n.d.	n.d.	n.d.	n.d.
Total	100.94	99.04	100.04	100.00	100.00	100.01	100.00	100.00	100.00	100.00
# Oxygens	12	3	1.75	4	4	24	4	6	3	6
Na	n.d.	n.d.	n.d.	n.d.	n.d.	5.42	0.58	n.d.	n.d.	n.d.
Mg	n.d.	n.d.	n.d.	0.47	0.48	0.21	0.07	0.25	n.d.	0.16
Al	0.09	0.04	0.01	1.08	1.92	5.20	0.83	0.71	0.08	1.28
Si	n.d.	n.d.	n.d.	n.d.	0.04	6.10	1.10	1.63	n.d.	0.82
Cl	n.d.	n.d.	n.d.	n.d.	n.d.	1.94	n.d.	n.d.	n.d.	n.d.
K	n.d.	n.d.	n.d.	n.d.	n.d.	n.d.	0.05	n.d.	n.d.	n.d.
Ca	0.31	0.87	0.12	0.51	0.02	0.16	0.07	1.13	0.87	0.95
Sc	3.01	0.05	0.22	0.07	n.d.	n.d.	n.d.	n.d.	n.d.	0.23
Ti	0.44	0.86	0.06	0.54	n.d.	0.29	n.d.	n.d.	0.90	0.35
V	0.03	0.01	0.00	0.03	n.d.	n.d.	n.d.	n.d.	n.d.	0.04
Cr	0.00	0.00	0.00	n.d.	n.d.	n.d.	n.d.	n.d.	n.d.	n.d.
Fe ^{*e}	0.07	0.01	0.01	0.03	0.54	0.36	0.09	0.29	0.02	0.03
Y	0.04	0.05	0.02	n.d.	n.d.	n.d.	n.d.	n.d.	0.09	n.d.
Zr	2.95	0.09	0.55	0.08	n.d.	n.d.	n.d.	n.d.	0.02	0.10
Hf	0.04	0.00	0.01	n.d.	n.d.	n.d.	n.d.	n.d.	n.d.	n.d.
Sum cations	6.99	4.98	1.00	2.81	3.00	17.74	2.79	4.01	1.99	3.96

^aHost phases of hexamolybdenum grain in USNM 3509HC12 (analysis given in Table 2).

^bErrors given inside parentheses are one standard deviation of the mean based on all of the analyses.

^cErrors given inside parentheses are one standard deviation computed from counting statistics.

^dn.d.: not determined.

^eAll Fe as FeO.

Table 2: Alloys in allendeite- and hexamolybdenum-bearing phase assemblages

Phase	hexamolybdenum grn#1	Ru-dominated region grn#1	hexamolybdenum grn#2	hexamolybdenum grn#3 (smallest)	Os-Ir-Mo-W grn#1	Os-Ir-Mo-W grn#2	Os-Ir-Mo-W grn#3	hexamolybdenum
Section	USNM 7554	USNM 7554	USNM 7554	USNM 7554	USNM 7554	USNM 7554	USNM 7554	USNM 3509HC12
type	EPMA ^a	EPMA	SEM-EDS ^b	SEM-EDS	SEM-EDS	SEM-EDS	SEM-EDS	EPMA
# analyses	6	2	1	1	1	1	1	8
Fe	4.27 (0.08) ^a	2.47 (0.01)	2.60 (0.30) ^b	1.98 (0.60)	1.71 (0.37)	2.32 (1.37)	2.35 (0.73)	11.84 (0.22)
Ni	0.47 (0.08)	0.29 (0.00)	n.d.	n.d.	n.d.	n.d.	n.d.	1.30 (0.13)
Mo	51.61 (0.46)	29.89 (1.18)	33.62 (0.88)	78.71 (2.29)	6.74 (0.91)	12.12 (1.99)	5.30 (1.21)	20.56 (0.36)
Ru	23.04 (0.63)	33.54 (0.43)	15.78 (0.72)	8.01 (1.45)	1.81 (0.73)	1.56 (1.41)	0.52 (1.03)	19.38 (0.46)
W	1.90 (0.26)	0.96 (0.09)	5.99 (0.57)	2.93 (1.00)	13.19 (0.89)	12.40 (1.59)	12.47 (1.28)	3.10 (0.16)
Re	n.d. ^c	n.d.	n.d.	n.d.	n.d.	n.d.	n.d.	0.96 (0.20)
Os	5.63 (0.66)	4.56 (0.39)	2.01 (1.11)	5.58 (1.48)	51.11 (1.44)	34.66 (2.72)	65.03 (2.18)	17.19 (0.75)
Ir	12.00 (0.81)	15.35 (1.26)	40.01 (0.94)	2.79 (1.34)	25.43 (1.26)	36.94 (2.53)	14.32 (1.82)	15.09 (0.92)
Pt	0.23 (0.38)	0.89 (1.26)	n.d.	n.d.	n.d.	n.d.	n.d.	0.07 (0.13)
Total	99.15	87.95	100.00	100.00	100.00	100.00	100.00	89.51
	Atomic %	Atomic %	Atomic %	Atomic %	Atomic %	Atomic %	Atomic %	Atomic %
Fe	8.01	5.48	5.78	3.57	5.17	6.64	7.17	25.50
Ni	0.84	0.61	n.d.	n.d.	n.d.	n.d.	n.d.	2.66
Mo	56.39	38.64	43.56	82.46	11.88	20.20	9.41	25.77
Ru	23.90	41.17	19.42	7.96	3.03	2.47	0.88	23.05
W	1.08	0.65	4.05	1.60	12.12	10.79	11.56	2.03
Re	n.d.	n.d.	n.d.	n.d.	n.d.	n.d.	n.d.	0.62
Os	3.10	2.97	1.32	2.95	45.42	29.15	58.28	10.87
Ir	6.55	9.90	25.88	1.46	22.37	30.75	12.70	9.44
Pt	0.12	0.58	n.d.	n.d.	n.d.	n.d.	n.d.	0.04
Sum	100.00	100.00	100.00	100.00	100.00	100.00	100.00	100.00

^aErrors given inside parentheses are one standard deviation of the mean based on all of the analyses.

^bErrors given inside parentheses are one standard deviation computed from counting statistics.

^cn.d.: not determined.

Table 3. Mineral names for $P6_3/mmc$ meteoritic alloys

Dominant element	Mineral name	Example	Reference
Os	Osmium	$Os_{0.35}Ir_{0.21}Mo_{0.20}W_{0.09}Ru_{0.08}Fe_{0.05}Re_{0.02}$	This study
Ir	Rutheniridosmine ^a	-----	-----
Ru	Ruthenium	$Ru_{0.38}Mo_{0.26}Fe_{0.26}Ni_{0.05}Pt_{0.03}Ir_{0.03}Os_{0.01}$	Harries et al. (2012)
Mo	Hexamolybdenum	$Mo_{0.56}Ru_{0.24}Fe_{0.08}Ir_{0.07}Os_{0.03}W_{0.01}Ni_{0.01}$	This study
Fe	Hexaferrum	$Fe_{0.55}Os_{0.15}Ir_{0.13}Mo_{0.08}W_{0.04}Ru_{0.02}Ni_{0.03}$	Ma (2012)
Ni	Garutiite ^a	-----	-----

^aThe existence of meteoritic garutiite and rutheniridosmine has not been confirmed. Ni-dominant and Ir-dominant alloys with concentrations of PGEs possibly sufficient to stabilize a $P6_3/mmc$ structure have been reported (e.g., Paque 1989; this study) but the structures of these grains have not been studied.

Table 4. Parameters for computing the vapor pressure of an element over the crystalline element in a $P6_3/mmc$ structure^a

element	A	B
Mo	33201	7.3991
W	44246	7.9608
Ir	34308	7.7100
Pt	29064	7.5936
Rh	28298	7.5415
Co	21393	6.9855
Ni	21447	7.0529
Fe	20532	6.9381
V	26489	7.6338

^aElemental Os, Re, and Ru assume stable $P6_3/mmc$ structures, so parameters for these elements are as given in Campbell et al. (2001).